Single Ion Addressing of up to 50 Ions

A master's thesis submitted to the

Faculty of Mathematics, Computer Science and Physics

of the

Leopold-Franzens University of Innsbruck

in partial fulfilment of the requirements for the degree of

Master of Science
(MSc.)

presented by

Lukas Falko Pernthaler

supervised by

o.Univ.-Prof. Dr. Rainer Blatt
and Dr. Christian F. Roos

carried out at the

Institute for Quantumoptics and Quantuminformation
(IQOQI)

August 2019

dedicated to my parents

Abstract

Quantum computers are believed to revolutionize the way of solving problems classical computers aren't able to. Related to the universal quantum computer, which can be programmed as wished, is the quantum simulator, which can be initialized with a certain problem or also only a single task of a greater problem. The problem is solved by evolving and measuring the state of the used qubits.
My work deals with a quantum simulator using linear chains of $^{40}Ca^{+}$ ions in a Paul trap. An optical setup was designed using the ZEMAX software to obtain an addressing range of more than 230 µm along with a spot size on the order of 2 µm for a 729 nm laser. This is achieved using an acousto-optical deflector (AOD) and an optical setup, which projects the output of the AOD on the focussing objective, while enlarging the laser beam at the same time. The system was characterized first in a test setup by putting a small-pixelsized CCD camera in the focal plane of the objective. Then, the old addressing system was replaced by the new one, allowing the addressability of 51 ions with comparable spot size of the 729 nm laser relative to the old setup. In the quantum simulation approach taken in this experiment, the ion transitions are addressed off-resonantly, in which case the beam spot was almost free of optical aberrations and the crosstalk of the center ion in a 51-ion chain was about 0.4 %.

Kurzfassung

Es wird erwartet, dass Quantencomputer die Art Probleme zu lösen, an denen klassische Computer scheitern, revolutionieren werden. Verwandt mit dem universellen Quantencomputer, welcher beliebig programmiert werden kann, ist der Quantensimulator, auf welchem ein gewisses Problem oder auch nur eine einzelne Aufgabe eines größeren Problems initialisiert werden können. Besagtes Problem wird dann durch Zeitentwicklung und Zustandsbestimmung der verwendeten Qubits gelöst.
Meine Arbeit handelt von einem Quantensimulator, unter Verwendung von linearen Ketten von $^{40}Ca^{+}$ Ionen in einer Paulfalle. Es wurde ein optischer Aufbau mit Hilfe der Software ZEMAX entworfen, um einen Addressierbereich von 230 µm zusammen mit einer Fokusgröße von 2 µm für einen 729 nm Laser zu erreichen. Dies wird mit Hilfe eines akusto-optischen Deflektors (AOD) und eines optischen Aufbaus erreicht, welcher den Ausgang des AODs auf das fokussierende Objektiv projeziert, während er zugleich den Laserstrahl aufweitet. Zunächst wurde ein Testaufbau mittels einer

CCD mit kleiner Pixelgröße charakterisiert, indem der Laserstrahl in der Brennebene des Objektivs analysiert wurde. Anschließend wurde der alte Addressierungsaufbau durch den neuen ersetzt, welcher die Addressierung von 51 Ionen mit vergleichbarer Fokusgröße des Laserstrahls, gemessen am alten Aufbau, erlaubte. Die Übergänge in den Ionen werden bei dieser Art der Quantensimulation dabei nicht resonant getrieben, welches einen Strahlfokus nahezu frei von optischen Aberrationen zur Folge hat, wobei das Übersprechen mit den Nachbarionen etwa 0.4 % oder geringer war.

Abbreviations

AC	alternating current
AMP	amplifier
AOD	acousto-optic deflector
AOM	acousto-optic modulator
CCD	charge-coupled device
eq.	equation
f.l.t.r	from left to right
fig.	figure
FWHM	full width half maximum
h.c.	Hermitian conjugate
PBS	polarizing beam splitter
resp.	respectively
RF	radio frequency
sec.	section

Contents

1. Introduction **7**

2. Theoretical concepts **9**
2.1. Paul traps . . . 10
2.1.1. Theory . . . 10
2.1.2. Ion in the linear string . . . 13
2.1.3. Paul trap design . . . 14
2.2. The $^{40}Ca^{+}$ ion . . . 14
2.3. Interactions between ions and light . . . 15
2.3.1. AC-Stark shift . . . 19
2.4. Basic optics . . . 19
2.4.1. Ray optics . . . 20
2.4.2. Gaussian beams . . . 21
2.5. Quantum simulation . . . 22
2.5.1. Basics . . . 23

3. Addressing setup **26**
3.1. AODs . . . 26
3.2. Simulation . . . 27
3.2.1. ZEMAX software . . . 27
3.2.2. Simulation results . . . 29
3.3. Setup . . . 30
3.4. Characterization of the AOD . . . 33
3.4.1. Diffraction efficiency . . . 33
3.4.2. Power dependence . . . 34
3.4.3. Response time . . . 35
3.5. Test setup . . . 35
3.5.1. Beam profile . . . 36
3.5.2. Spot size . . . 36
3.5.3. Multiple frequency input . . . 38
3.5.4. Addressing range . . . 39
3.5.5. Comparison between old and new setup . . . 40

4. 50 ion addressing **41**
4.1. Building process . . . 41
4.2. 51 addressed ions . . . 41
4.2.1. Pulse sequence . . . 42

4.3. Focal spot 43
4.3.1. Beam shape 43
4.3.2. Spot size 45
4.4. Crosstalk 48
4.5. Observation of beat signal 54

5. Conclusion and outlook **55**

Appendices **61**

A. Rabi flops in a 10 ion chain **62**

B. Datasheet AOD **65**

1. Introduction

Science and technology never developed as fast as in the last decades. Nevertheless, many developments and discoveries made centuries ago are still of fundamental importance not only for the field of physics, but science in general.
Almost every time a physical experiment is performed, some theory or simulation is about to be proved or disproved. In ancient times the required calculations for these theories were mostly made by hand or with the help of simple but quite efficient tools like the abacus. With the introduction of differential and integral calculus by Newton and Leibniz, the complexity of calculation increased drastically and for a long time scientists could describe phenomena mathematically, but couldn't solve the regarding equations. This changed with the development of the computer in the middle of the last century, as proposed by Alan Turing [1]. With increasing speed and memory of the computers, more and more problems became solvable.
At the same time, there were also major developments in the field of quantum theory, introduced Heisenberg [2] and Schrödinger [3]. Soon it became clear, that problems in quantum mechanics could be simulated exactly with a classical computer only up to a certain limit, which means in most cases up to a certain number of quantum particles in the system. In 1981, Richard Feynman proposed in his famous lecture [4] to use devices on the basis of quantum mechanics to solve quantum mechanical problems, which inspired a variety of research groups to work towards the goal of a quantum computer. In 1996 resp. 1997, Lov Groover and Peter Shor showed in their work [5] resp. [6], that quantum computers (quantum processors) were not only useful for the simulation and solution of quantum mechanical problems, but also for computationally hard classical problems, that are of more general interest for the public. It didn't take much time after the first announcement of the Shor algorithm in 1994 before Cirac and Zoller [7] showed in their theoretical work a possible experimental realization of a quantum computer using trapped ions. A few years later, there was the first experimental realization of the Cirac-Zoller CNOT-gate (CZ-gate) in the group led by Rainer Blatt in Innsbruck [8]. The quantum CNOT operation is a quantum gate that is the quantum analogue of a controlled-not operation on a classical computer. It is one of the quantum gates on whose basis one can construct a universal quantum computer.
Shor's algorithm was realized the first time in 2001 [9] to factorize 15 in its prime factors 3 and 5 using ensembles of 7 spin 1/2 nuclei in a molecule, whose states were controlled using magnetic resonance techniques. In trapped-ion implementations of quantum computing, the first quantum byte, containing 8 entangled $^{40}Ca^{+}$ quantum bits [10], was realized in 2005, before enlarging this number to 14 in 2011 [11].
The use of a computer based on qubits, quantum bits in the form of e.g. a two-level

atom, permits for some computational tasks the storage and processing of information with exponential advantage in comparison to a classical computer. In a classical computer, the information is built up by storing it as zeros and ones in the basic unit of information, the bit, whereby a qubit can take a variety of different states, a so-called superposition of the two basis states $|g\rangle$ and $|e\rangle$. On the trapped-ion platform, the qubit is encoded in electrical levels of a suitable ion. At the moment, there is still a long way to go towards an universal quantum computer, still experiments show the possibility of such a device being constructed in the near future.
In this thesis an optical system for the addressing of a chain of 50 $^{40}Ca^{+}$ ions is described. In chapter 2, an introduction to the theoretical background is given, from ion traps over optics to quantum simulation. The simulations for the addressing setup and the setup itself are described in chapter 3, along with the characterization of the acousto-optical deflector (AOD) used in the setup and a test system. At the end, in chapter 4, the addressing system is characterized in terms of beam shape and crosstalk in the actual experiment by using the best sensors, namely the ions themselves. As a conclusion, the main results of the thesis are summarized and an outlook is given in chapter 5.
In the appendix A, one can find plots for the specification of a 10-ion chain as well as the data sheet of the AOD used in the setup in appendix B.

2. Theoretical concepts

Different physical systems have been identified as suitable as a basis for performing quantum simulations. Besides ions that are held in traps and manipulated and measured with laser light, which will be treated further in the following section, one can also think of quantum simulators using superconducting qubits, as used by most of the big players on the field, like Google, IBM or Intel [12], or ultracold atoms in optical lattices[13, 14]. In order to generalize some important requirements fro performing quantum computation, in 2000 David DiVicenzo [15] famously formulated five (plus two) criteria required for doing universal quantum computation. These were:

1. A scalable physical system with well characterized qubits
2. The ability to initialize the state of the qubits to a simple fiducial state
3. Long relevant decoherence times, much longer than the gate operation times
4. A universal set of quantum gates
5. A qubit-specific measurement capability
6. The ability to interconvert stationary and flying qubits
7. The ability faithfully to transmit flying qubits between specified locations

The latter two criteria are important for doing quantum communication, which is not so important for the purpose of quantum simulation. In the case of trapped ions, the first five criteria are mostly fulfilled: ions can be addressed with high fidelity and the coherence time is on a much longer then the gate operation time [16]. There also exist gates for trapped ions, like the Cirac-Zoller gate [7] and the Mølmer-Sørensen gate [17], which allow for universal gate operations. In our case of $^{40}Ca^{+}$, the state of the qubit can be determined quite easily exciting transitions and collecting fluorescence light. The only problem trapped ions face is the scalability. Whereas one can e.g. industrially produce large number of superconducting qubits using microfabrication techniques or trap thousands of atoms in optical lattices, the number of trappable and individually controllable ions is limited so far to a few tens [18]. To understand why, one has to get a deeper insight into the physics of ion traps, in this case the Paul trap. In this section, I will try to give this insight, before I will discuss properties of the calcium ion, which acts as a qubit, give a brief introduction to ray optics and ion-light interaction and come to the application for quantum simulation.

2.1. Paul traps

When conducting experiments with ions, one can choose between a few frequently used and well known trapping solutions. There is the possibility to trap ions using magnetic and electric fields, as in the Penning trap [19], or just electric fields, as in the Paul trap [20]. These types of ion traps are very often used not only in the field of quantum physics, but also in a variety of different fields, where their purpose is mostly the one of mass filters in mass spectrum analysers [21].
I will first describe the theoretical framework of a Paul trap, before I will shortly describe the trap used in the quantum simulation experiment.

2.1.1. Theory

The usual way of trapping something in real life is keeping it confined in every direction. If we consider for example a bowl filled with water, the bowl confines the water on the bottom and the sides, whereas gravity prevents the water from pouring out at the top. The same principle works also for ions, which can be trapped in a stable way only by using potentials with a positive curvature, e.g. caused by an electrostatic potential. Gravity doesn't qualify as trapping potential, since the Coulomb force (e.g. between two ions) is many orders of magnitude stronger than gravity. Therefore gravity can be neglected (and therefore not used as a means of trapping) in this case. So lets consider electrostatic potentials: If one puts an electrical potential barrier $\phi(x, y, z)$ in all three spatial directions x, y and z, the ion should be unable to escape. But there is a fundamental problem, which arises in the form of the Earnshaw theorem[22], which has in this case the form of the Laplace equation

$$\Delta\phi(x, y, z) = \frac{\partial^2\phi}{\partial x^2} + \frac{\partial^2\phi}{\partial y^2} + \frac{\partial^2\phi}{\partial z^2} = 0 \tag{2.1}$$

This means, that in at least one spatial direction, the curvature of the electrostatic potential has to be negative, which indicates, that the trapping in this spatial direction is unstable. Paul solved this problem using dynamic electric fields. In his Nobel lecture [23], Paul explained the effect using a rotating saddle surface and a ball: Whenever the ball is about to roll down the negatively part of the surface, it is pushed back to the saddle point by the positively curved part of the surface, which has in the meantime rotated in the place of the negatively curved one. A look to fig. 2.1 may clarify this analogy further.

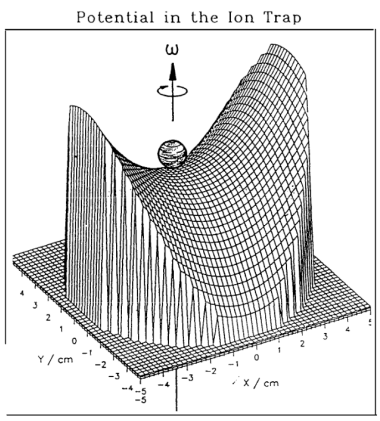

Figure 2.1.: Mechanical analogue of a Paul trapping potential, taken from [23].

The following paragraphs follow the argument (and the notation) given in the Nobel lecture of Paul [23]. In the first approximation, the force F, confining an

ion, increases linearly with the distance $|\vec{r}| = r$ at the location $\vec{r}$ from the trap center, so as to say

$$F = -ar \tag{2.2}$$

with $a > 0$. The force is hereby a restoring force, since it is pushing the ion back. Integrating this equation leads to a potential ϕ of the form

$$\phi(x, y, z) \propto (\alpha x^2 + \beta y^2 + \gamma z^2) \tag{2.3}$$

with α, β and γ constants. It is very often, like for us, the case, that there are electric quadrupoles used to generate a potential ϕ_{quad} like in eq. 2.3, which then has the form

$$\phi_{quad} = \frac{\phi_0}{2r^2}(\alpha x^2 + \beta y^2 + \gamma z^2) \tag{2.4}$$

with ϕ_0 a constant and r the distance from the symmetry axis. In order to fulfil the Laplace equation 2.1, one can either choose trivially $\alpha = 1$, $\beta = 0$ and $\gamma = -1$, which corresponds to a 2-dimensional confinement in x and z direction, or a three-dimensional confinement, which can be achieved choosing $\alpha = 1$, $\beta = 1$ and $\gamma = -2$. Considering the former case, corresponding to a mass filter, one obtains a potential of the form

$$\phi(x, y, z) = \frac{\phi_0}{2r_0^2}\left(x^2 - z^2\right) \tag{2.5}$$

Such a potential can be achieved approximately using 4 parallel metal rods, the exact potential can be achieved using hyperbolically formed metal plates. The problem with this configuration is, as already explained above, that if now some ions enter the configuration on the center axis, they are unstable in either the x or the z direction, depending on their charge, since 2 opposite electrodes will attract them. If the ions move a tiny bit out of the center axis, they get accelerated towards the electrode they are closer to, and are lost. One can overcome this problem, in analogy to fig. 2.1, by applying an additional periodic potential of the form

$$\phi_0 = U + V\cos(\Omega_{RF}t) \tag{2.6}$$

with amplitude V, frequency Ω_{RF} and time t, besides the static potential U. By taking the gradient of the potential and multiplying with the charge e of the ion, one gets the equations of motion of the form

$$\begin{aligned} \ddot{x} + \frac{e}{mr_0^2}\left(U + V\cos(\Omega_{RF}t)\right)x = 0 \\ \ddot{z} - \frac{e}{mr_0^2}\left(U + V\cos(\Omega_{RF}t)\right)z = 0 \end{aligned} \tag{2.7}$$

with m the mass of the ion. Taking a closer look on the time-varying term, one may come to the conclusion, that the resulting force averages out with time. However, this is not the case, since the force is not only dependent on time, but also on space, meaning that the repelling force is smaller when the particle closer to the center than

the restoring force when it is farther away from the center. One can show this using the so-called secular approximation. Considering only the x-direction, this amounts to splitting the variable describing the position of the ion $x(t)$ into a slowly varying part $\bar{x}(t)$ and a fast oscillating part $\chi(t)$, meaning $x(t) = \bar{x}(t) + \chi(t)$. One can now first solve the fast oscillating part of the equation of motion

$$m\ddot{\chi} = F(\bar{x}, t) \tag{2.8}$$

at the location $\bar{x}$, since $\bar{x}$ changes much slower than χ and can therefore be considered as constant. The force is in this case the Coulomb force $F_C = e\nabla\phi_0$, taking into consideration the oscillating part of eq. 2.6, this leads to

$$\chi(t) = \frac{eV}{mr_0^2\Omega_{RF}^2}\bar{x}\cos(\Omega_{RF}t) \tag{2.9}$$

Now, the force for the slowly-varying part at the position $\bar{x}(t)$ corresponds to the average force over time, so as to say $m\ddot{\bar{x}}(t) = \langle F(x,t)\rangle$. Substituting x by $\bar{x}(t) + \chi(t)$, one obtains

$$\langle F(x,t)\rangle = -\frac{e^2V^2}{2mr_0^4\Omega_{RF}^2}\bar{x}. \tag{2.10}$$

So what we obtain in total is a restoring force pushing the ion to the center when averaged over one period of the oscillating signal. This approximation is valid if the resulting harmonic motion has a frequency much smaller than the drive frequency.
The difference from taking only into consideration the RF-potential in eq. 2.6 to the term with the applied DC potential is, that the confining potential is lowered in one trapping direction and raised in another. By tuning the amplitudes U and V, one can achieve, that only ions with a certain charge-to-mass ratio make it through the mass filter. If one applies now also a static potential of the form of eq. 2.4 with $\alpha = \beta = 1$ and $\gamma = -1$, one can trap ions in a linear string.
Coming back to eq. 2.7, one may see that those equations have the form of the so-called Mathieu equations [24], which are often written as

$$\begin{aligned} \frac{d^2x}{d\tau^2} &= -\left(a + 2q\sin(2\tau)\right)x \\ \frac{d^2z}{d\tau^2} &= \left(a + 2q\sin(2\tau)\right)y \end{aligned} \tag{2.11}$$

with

$$\tau = \frac{\Omega_{RF}}{2}t, \qquad q = \frac{2eV}{mr_0^2\Omega_{RF}^2} \qquad \text{and} \qquad a = \frac{4eU}{mr_0^2\Omega_{RF}^2} \tag{2.12}$$

Solving eq. 2.11, one obtains oscillations with frequencies

$$\omega_x = \frac{\Omega_{RF}}{2}\sqrt{\frac{q^2}{2} + a} \qquad \text{and} \qquad \omega_z = \frac{\Omega_{RF}}{2}\sqrt{\frac{q^2}{2} - a}, \tag{2.13}$$

which means that stable solutions can be only obtained if $a > -\frac{q^2}{2}$ in the case of ω_x and $a < \frac{q^2}{2}$ in the case of ω_z, resulting in a region of stability shown in fig. 2.2. The behaviour for large q is hereby not covered, since the secular approximation doesn't hold in that case.

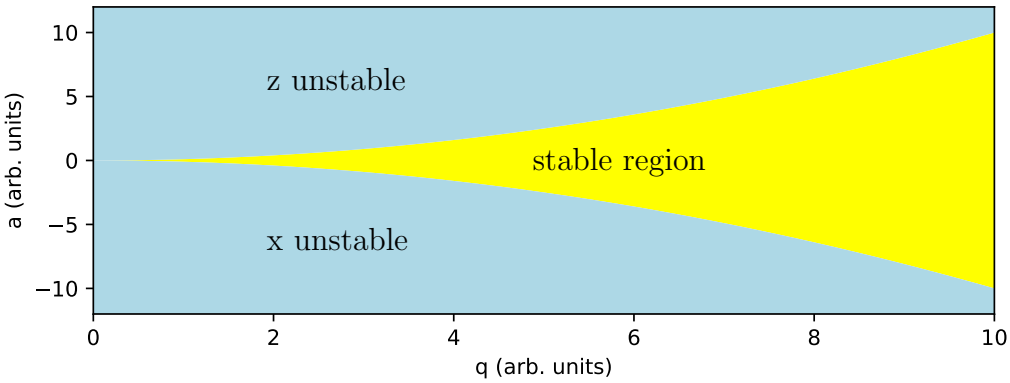

Figure 2.2.: Stability diagram for the Mathieu equations 2.11 as function of the a and q-parameter. The stable region is marked in yellow, the unstable in blue.

2.1.2. Ion in the linear string

This section is based on the 1998 paper by D.F.V James [25]. Ions in a linear Paul trap underlay two main forces: The restoring Coulomb force, generated by the trapping potential, confining in all three dimensions, and the repelling Coulomb force, caused other ions in the trap and acting along the longitudinal dimension of the trap (if the ions form a linear string). Since the potential in the longitudinal direction is very weak

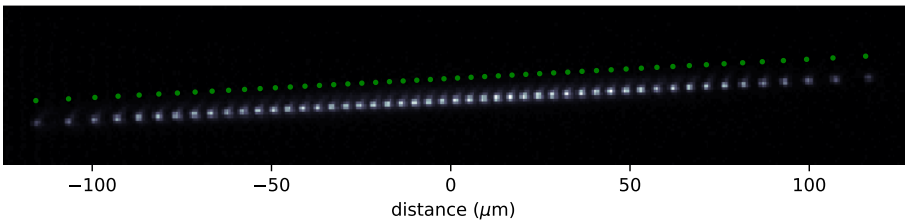

Figure 2.3.: Camera picture of a 50 ion chain overlaid with the calculated theoretical position (green dots). The scale was converted from pixel to µm, whereby the picture was taken with an applied tip voltage of 12 V at the Paul trap.

in comparison to the one in the radial direction, one can neglect the motion along this directions. The potential V_{trap} one obtains is therefore

$$V_{trap} = \sum_{m=1}^{N} \frac{1}{2} m\omega^2 x_m(t)^2 + \sum_{\substack{n,m=1 \\ m\neq n}}^{N} \frac{e^2}{8\pi\epsilon_0} \frac{1}{|x_n(t) - x_m(t)|} \tag{2.14}$$

with N the total number of ions in the ion chain, ω the longitudinal trap frequency, $x_m(t)$ the position of the mth ion and ϵ_0 the permittivity of free space.
In fig. 2.3 the camera image of an actual 50 ion chain, which was generated with a code

written by Christine Maier out of the raw camera data, is overlaid with the calculated theoretical values using eq. 2.14. As one can see, the actual position matches well with the calculated one.

2.1.3. Paul trap design

The current trap used in the experiment is from the second generation of linear Paul traps at the University of Innsbruck/IQOQI, designed and manufactured by Stefan Haslwanter [26]. A picture of the trap is shown in fig. 2.4. It consists of two tip electrodes, confining the ions in the longitudinal direction. Those electrodes have holes in their center, allowing for a beam to target the ion chain. The tip electrodes are surrounded by four RF blade electrodes, which confine the ions transversally. Furthermore, there are compensation electrodes built into the trap, to compensate for electrical stray fields. The trap sits in a UHV chamber with pressures below 10^{-10}mbar. The trap and the whole chamber are also actively magnetically stabilized with large coils surrounding the chamber.

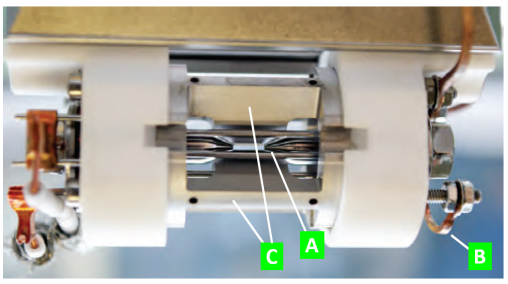

Figure 2.4.: Second generation Paul trap at the IQOQI Lab 1. It consists of 2 tip electrodes (A), surrounded by 4 RF blade electrodes (C). The connection between the opposite electrodes can be seen at the bottom right corner (B). The picture (modified) was taken from [26].

2.2. The $^{40}Ca^{+}$ ion

After having discussed the Paul trap, I will present some properties of the ion species used in the experiments, i.e. $^{40}Ca^{+}$.
Calcium is part of the group of alkali earth metals, the second main group in the periodic table. Therefore, it has two valence electrons in its outermost shell. For encoding a qubit, it is convenient to use an ion species with a single valence electron as such ions have comparatively simple level schemes with transition wavelength in a wavelength range that can be conveniently accessed by lasers. In the experiment, the neutral calcium atom is vaporized by applying current to a solid piece of it. The problem is hereby, that the calcium isotope used in this experiment (^{40}Ca) has a natural abundance of 96.6 % [27]. This means, that within a chain of 50 ions, there would be 2 ions with different mass. This difference in mass shifts the transitions within the ion frequency-wise. This problem is solved by using an isotope-sensitive ionisation process. First, one valence electron is pushed to the 4s4p $^{1}P_{1}$ level, using a 423 nm laser, before being punched out of the atom using a 375 nm laser [26]. For the other isotopes, the first ionization step is not resonant to any energy level, which prevents an excitation of the atom. Also, the second step doesn't provide enough energy to ionize a calcium isotope. That way, one creates a pure string of $^{40}Ca^{+}$ ions

out of the ionization process.

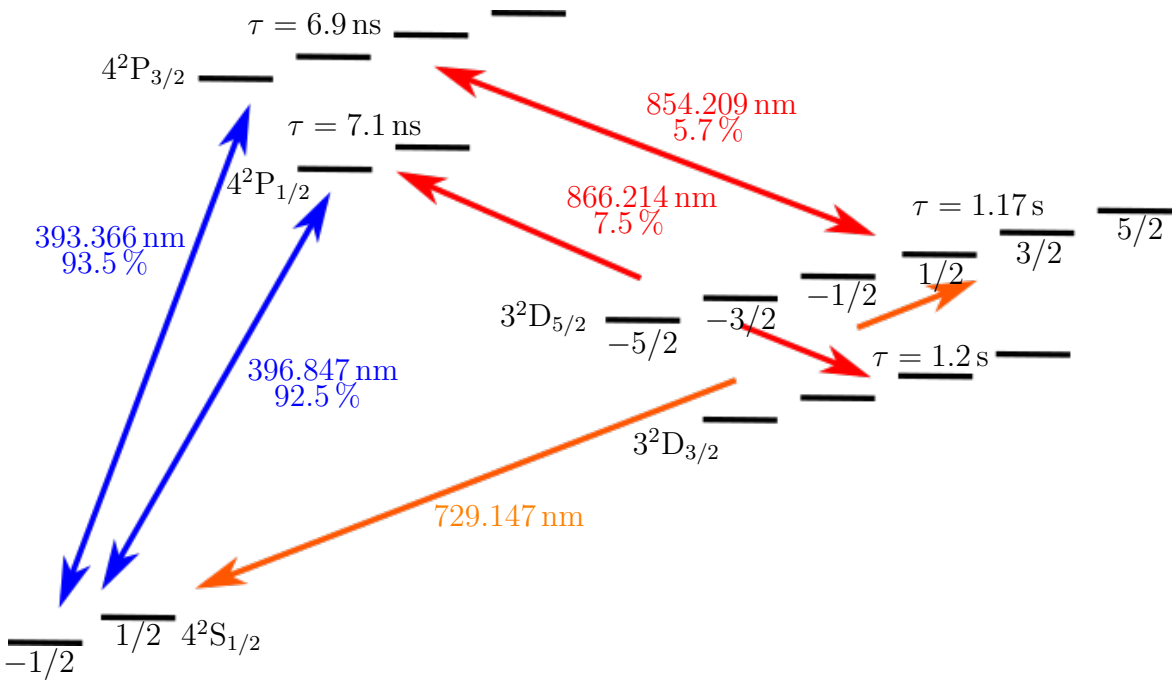

Figure 2.5.: Wavelengths and lifetimes of the relevant transitions and energy levels in the $^{40}Ca^+$ ion. The remaining 0.8 % from the $4^2P_{3/2}$ level go to the $3^2D_{3/2}$ level. Adapted from [28]

The ground state of the $^{40}Ca^+$ ion is the $4^2S_{1/2}$ state. The two most important transitions are on the one hand the qubit transition to the $3^2D_{5/2}$ state, due to its long lifetime of 1.17 s, and on the other hand the dipole transition to the $4^2P_{1/2}$ level, used for Doppler cooling and imaging. It is suitable for Doppler cooling, since it has a quite broad linewidth of about 22.4 MHz [26], allowing for a rapid cooling of the ion. The imaging is done by shining resonant 397 nm light on the ions, exciting the $4^2S_{1/2}$ to $4^2P_{1/2}$ transition. If the ion is in its ground state, it will emit 397 nm fluorescence light, which is detected by a CCD camera. If the ion is in the exited $3^2D_{5/2}$ state, no excitation will happen and therefore no fluorescence light be shone to the CCD; therefore, when the ion is in the excited state, it remains dark. Repumping from the $3^2D_{5/2}$ level and the $3^2D_{5/2}$ level to the ground state is done with lasers emitting at 866 nm and 854 nm, respectively. A full scheme with all relevant transitions, their according wavelengths and lifetimes is shown in fig. 2.5.

2.3. Interactions between ions and light

The easiest and most efficient way to manipulate ion states is by lasers. In this section, a theoretical framework on the basis of quantum mechanics will be described. This section is based upon chapter 3 in [29].

The ion is assumed to be trapped in a three dimensional harmonic potential, which has the form $\frac{1}{2}m\omega_i^2 x_i^2$ in every dimension i, which is approximately the case for not too large displacements. In the longitudinal direction, the trap frequency is of course different from the transversal direction. The Hamiltonian of the ion, regarding just one spatial dimension, has then the form

$$H_0 = \frac{p^2}{2m} + \frac{1}{2}m\omega^2 x^2 + \frac{1}{2}\hbar\nu\sigma_z. \tag{2.15}$$

Here, the first two terms represent the kinetic and potential energy of the particle with p the momentum of the ion. The last term accounts for the energy stored in the two energy levels comprising the qubit with $\hbar$ the reduced Planck constant, $\hbar\nu$ the energy difference between the two levels in the ion and σ_z the Pauli Spin-z-matrix.
Now the interaction with the laser filed comes into play. It can be expressed as

$$H_1 = \frac{1}{2}\hbar\Omega(\sigma^+ + \sigma^-)\left(e^{i(kx-\nu_L t+\phi)} + e^{-i(kx-\nu_L t+\phi)}\right) \tag{2.16}$$

with σ^+ and σ^- the atomic raising and lowering operators, Ω the Rabi frequency resp. coupling strength, $k = \frac{2\pi\nu_L}{c}$ the laser wave number, ν_L the frequency of the laser field and ϕ its phase. The constant c describes hereby the speed of light. An applied atomic raising operator pushes the ion's valence electron to the excited level $|e\rangle$, the atomic lowering operator kicks it down to the ground state $|g\rangle$. They raising and lowering operators are defined as

$$\sigma^+ = |e\rangle\langle g| \quad \text{and} \quad \sigma^- = |g\rangle\langle e| \tag{2.17}$$

The sum

$$H = H_0 + H_1 \tag{2.18}$$

is then the total Hamiltonian describing the system. Making use of the creation and annihilation operators $\hat{a}$ and $\hat{a}^\dagger$ introduced by Dirac [30] and defined as

$$\hat{a} = \sqrt{\frac{m\nu}{2\hbar}}\left(\hat{x} + \frac{i}{m\nu}\hat{p}\right) \quad \text{and} \quad \hat{a}^\dagger = \sqrt{\frac{m\nu}{2\hbar}}\left(\hat{x} - \frac{i}{m\nu}\hat{p}\right) \tag{2.19}$$

with $\hat{x}$ and $\hat{p}$ the position and momentum operators, one can rewrite eq. 2.15 and eq. 2.16 as

$$H_0 = \hbar\omega\left(\hat{a}^\dagger\hat{a} + \frac{1}{2}\right) + \frac{1}{2}\hbar\nu\sigma_z \tag{2.20}$$

$$H_1 = \frac{1}{2}\hbar\Omega\left(e^{i\eta(\hat{a}+\hat{a}^\dagger)}\sigma^+ e^{-i\nu_L t} + e^{-i\eta(\hat{a}+\hat{a}^\dagger)}\sigma^- e^{i\nu_L t}\right) \tag{2.21}$$

with the Lamb-Dickie parameter

$$\eta = kx_0 = k\sqrt{\frac{\hbar}{2m\omega}} \tag{2.22}$$

and $\hat{x} = x_0(\hat{a} + \hat{a}^\dagger)$.
Here the Lamb-Dickie parameter is a means to compare the laser wavelength $\lambda = \frac{2\pi}{k}$ to the ground state size $x_0 = \sqrt{\frac{\hbar}{2m\omega}}$ of the ion. In its squared form, the Lamb-Dickie parameter can also be seen as a comparison between recoil energy $E_{rec} = \frac{(\hbar k)^2}{2m}$ and the harmonic oscillator level spacing $\hbar\omega$ in the trapping potential, saying $\eta^2 = (kx_0)^2 = \frac{E_{rec}}{\hbar\omega}$.
In the case of eq. 2.21, the rotating wave approximation was applied, omitting the fast oscillating terms, which average out quickly to 0. Going to the interaction picture $H_I = U^\dagger H U$ with $U = e^{iH_0 t/\hbar}$, the total Hamiltonian 2.18 becomes

$$H_I = \frac{\hbar\Omega}{2}\left(\sigma^+ e^{-i\Delta t} \cdot e^{\left(i\eta\left(\hat{a}e^{-i\omega t} + \hat{a}^\dagger e^{i\omega t}\right)\right)} + h.c.\right) \tag{2.23}$$

with Δ the detuning of the laser frequency from the transition frequency from the ground to the excited state ν

$$\Delta = \nu_L - \nu \tag{2.24}$$

For small η, one can approximate

$$e^{\left(i\eta\left(\hat{a}e^{-i\omega t} + \hat{a}^\dagger e^{i\omega t}\right)\right)} \approx 1 + i\eta\left(\hat{a}e^{-i\omega t} + \hat{a}^\dagger e^{i\omega t}\right) + \mathcal{O}(\eta^2) \tag{2.25}$$

Inserting eq. 2.25 into eq. 2.23, one gets three different terms: Where $\Delta = 0$, resonant excitation occurs, the Hamiltonian has the form

$$H_{car} = \frac{\hbar\Omega}{2}\left(\sigma^+ + \sigma^-\right) \tag{2.26}$$

This type of interaction is said to be on the carrier transition. This means, the ion is excited without changing the motional quantum state n in the trap. The quantum number n is hereby the expectation value of the so called phononic number operator $\hat{n} = \hat{a}^\dagger\hat{a}$, which gives the number of energy quanta $\hbar\omega$ the ion has in the trap.
For $\Delta \neq 0$, there are two important cases: One can either go to the so called blue or red sideband by setting the detuning to either $\Delta = \omega$ or $\Delta = -\omega$, as depicted in fig. 2.6. For this kind of excitation, the coupling strength changes, for the red sideband to $\Omega_{red} = \eta\sqrt{n}\Omega$ and for the blue sideband to $\Omega_{blue} = \eta\sqrt{n+1}\Omega$. The Hamiltonians have the form

$$H_{red} = \frac{i\hbar\eta\sqrt{n}\Omega}{2}\left(\hat{a}\sigma^+ - \hat{a}^\dagger\sigma^-\right) \tag{2.27}$$

$$H_{blue} = \frac{i\hbar\eta\sqrt{n+1}\Omega}{2}\left(\hat{a}^\dagger\sigma^+ - \hat{a}\sigma^-\right) \tag{2.28}$$

On the red sideband, one can either lower the phononic quantum number by 1 and excite the ion, or deexcite the ion while enhancing the phononic quntum number by 1. On the blue sideband, one can either excite the ion and enhance the phononic quantum number by 1 or deexcite the ion and decrease the phononic quantum number by 1.

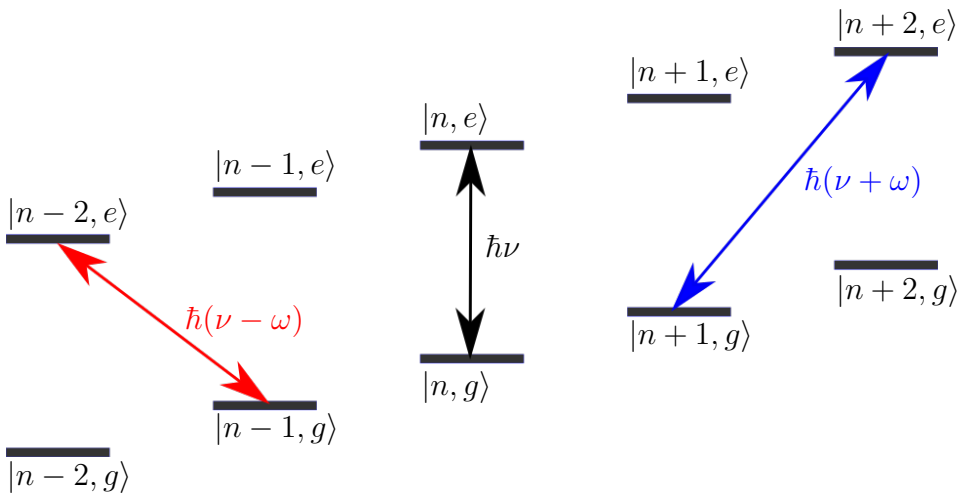

Figure 2.6.: Scheme of the energy structure of a 2-level ion in a harmonic potential. The first quantum number of the states is the phononic quantum number, the second quantum number is the quantum number describing the inner state of the ion. Hereby g describes the ground state and e the excited state. An example for a carrier transition is depicted in black, one for the red sideband transition in red and one for the blue sideband in blue.

On narrow transitions one always realizes maximum one of those three transitions. As one may see, the red sideband can be used to cool the ion to its motional ground state. To achieve this, the excited state has to decay fast to the ground state, like it is the case for the 397 nm transition (see fig. 2.5).
When running resonant excitations at $n = 0$, the population of the ground state resp. the excited state exhibit so-called Rabi oscillations as a function of the length of the exciting pulse. Those oscillations can be derived solving the optical Bloch equations [31] for a 2-level system. For a ground state population $p_g = 1$ at time $t = 0$, one gets a time-dependent population of ground (p_g) and excited state (p_e)

$$p_g(t) = \cos^2\left(\frac{\Omega t}{2}\right) \quad \text{and} \quad p_e(t) = \sin^2\left(\frac{\Omega t}{2}\right) \tag{2.29}$$

where the Rabi frequency Ω is

$$\Omega = \frac{\vec{d}_{ge}\vec{E}}{\hbar} \tag{2.30}$$

with $\vec{d}_{ge}$ the dipole matrix element of the transition from ground to excited state and $\vec{E}$ the electric field caused by the laser.
In reality, there is often more than just one motional mode occupied, which leads to a decay of the Rabi oscillations. This decay process can be approximately described (see derivation in [29]) for the excited state population via

$$p_e(t) \approx \frac{1}{2}\left(1 - \frac{\cos(2\Omega t) + 2\Omega t\eta^2(\bar{n}+1)\sin(2\Omega t)}{1 + (2\Omega t\eta^2(\bar{n}+1))^2}\right) \tag{2.31}$$

with $\bar{n}$ the mean phonon number.

2.3.1. AC-Stark shift

Up to now, the laser beam has been described to be more or less in resonance with the transition in the ion. To get maximum efficiency, usually one tries to get as close to the transition frequency as possible. Now there is an effect [32] described, which tunes the laser frequency far off (for the used qubit transition it is on the order of a few tens of Megahertz) the transition in the ion. Far off means hereby, that the transition is still excited, but with a lower probability. The following argument is based on [29].
Considering a laser beam coupling off-resonantly to a carrier transition, the transition is shifted energetically by an amount

$$\delta_{AC} = -\frac{\Omega^2}{2\Delta} \tag{2.32}$$

with $\Delta = \nu_L - \nu$ the detuning of the laser. This means, if one shines in a red-detuned laser beam, meaning a laser beam with a lower frequency than the transition frequency, to the carrier transition, the transition is spaced further apart and vice versa. Hereby, the spacing splits up equally on both levels. In the red-detuned case, the upper level is shifted upwards by $\frac{\Omega^2}{4\Delta}$ and the lower level downwards by $\frac{\Omega^2}{4\Delta}$. Also, the coupling is affected by the detuning. The occupation of the excited state can be described as [33]

$$p_e(t) = \frac{\Omega^2}{\Omega^2 + \Delta^2} \sin^2\left(\frac{\sqrt{\Omega^2 + \Delta^2}t}{2}\right) \tag{2.33}$$

This means, that the population doesn't go all the way to 1 any longer, whereby the oscillation period becomes shorter. The effective Rabi frequency $\tilde{\Omega}$ changes to

$$\tilde{\Omega} = \sqrt{\Omega^2 + \Delta^2} \tag{2.34}$$

The biggest advantage is, that the coupling is now proportional to the square of the Rabi frequency, which also means proportional to the square of the electric field. For the purpose of addressing single ions positioned very closely to each other, this is a major advantage, since the beam diameter the ions see, reduces by a factor of $\sqrt{2}$ with respect to resonant excitations. Also, in this case, one doesn't have to worry about the right phase of the laser beam any longer.

2.4. Basic optics

Optical know-how is needed to allow for precise addressing of single ions with tiny spot-sized laser beams. If a laser beam is focussed with very small spot size on a well-located ion, one doesn't need high laser powers to manipulate the state of the ion in a reasonable time. Also, when going to longer chains of ions, the distance between them becomes smaller and smaller, which makes a small laser spot size necessary in order to not affect neighbouring ions when shooting at one ion.
First of all, ray optics are introduced, before going to Gaussian optics, whose description contains some important definitions for the determination of the spot size of a focussed laser beam.

2.4.1. Ray optics

Ray optics are the most basic description of light propagation. Nevertheless, for the purpose of designing an optical setup, ray optics is the first step of getting an idea how the setup should look like. This section is based on chapter 1 in [34].
If light propagates through a medium or through an object, whose size is much bigger than the light's wavelength, the light can be described in good approximation as a ray. These rays obey some quite simple geometrical rules.
First of all, light travels through a medium with a certain index of refraction $n(r)$. For vacuum, the index of refraction is $n = 1$, for other media $n \geq 1$. Also, the propagation speed of light c is dependent on the index of refraction

$$c = \frac{c_{vac}}{n} \tag{2.35}$$

where c_{vac} is the speed of light in the vacuum. A very important point, when it comes to the design of an optical setup, is, that the spatial and optical pathlength of light are different. Considering a spatial distance d, the optical distance the light travels corresponds to $n \cdot d$. The path the light takes in a medium with index of refraction $n(\vec{r})$ from a point A to a point B is determined by Fermat's principle

$$\delta \int_A^B n(\vec{r}) ds = 0 \tag{2.36}$$

meaning that the light takes the path through the medium for which the optical pathlength is minimized. Using eq. 2.36, one can deduce the law of reflection and Snell's law. The law of reflection states, that if a light ray is reflected from a surface, its angle of incidence θ_i and angle of reflection θ_r are the same

$$\theta_i = \theta_r \tag{2.37}$$

and that the reflected rays lay in the plane of the incident rays. Snell's law comes into play, whenever light propagates at the boundary between two materials with different index of refraction n_1 and n_2. For an angle of incidence θ_1, the angle of refraction θ_2 obeys

$$n_1 \sin(\theta_1) = n_2 \sin(\theta_2) \tag{2.38}$$

Making use of a mirror or a lens, light beams can be focussed or expanded. The distance, at which the beam is focussed, is the so called focal length f. When positive, a collimated beam is focused at a distance f from the lens, when negative, a collimated beam is expanded after the lens, as if it was expanding from a focus at a distance $-f$ behind the lens. Here, collimation means that the rays the beam consists of, are oriented approximately parallel and barely diverge.
Rays that are not far away from the optical axis, i.e. the axis the optical components are centred around, are called paraxial rays. For paraxial rays and when propagating through a focussing element with focal length f, a point P_1 a distance z_1 away from

the optical axis, is imaged to a point P_2, which is separated by a distance z_2 from the optical axis. Hereby, the so-called imaging equation

$$\frac{1}{z_1} + \frac{1}{z_2} = \frac{1}{f} \tag{2.39}$$

holds.

2.4.2. Gaussian beams

Whenever a beam is focussed, the behaviour in and around the focus can't be treated any longer using ray optics, since in the latter case the size of a paraxially incoming beam would be infinitesimally small in the focus. Since this is not the case, one has to come up with an extended theory. In this section, the concept of Gaussian beams is introduced together with some important properties and definitions. This section is based upon chapter 3 in [34].
The Gaussian beam is not only a very common case of light propagation, like for example for the output of a laser, but also the solution of the paraxial Helmholtz equation

$$\nabla_T^2 A - 2ik\frac{\partial A}{\partial z} = 0 \tag{2.40}$$

with A the complex envelope, $\nabla_T^2 = \frac{\partial^2}{\partial x^2} + \frac{\partial^2}{\partial y^2}$ the transverse Laplacian operator and k the wave vector.
A general Gaussian beam $U(\varrho, z)$ has the form

$$U(\varrho, z) = A_0 \frac{w_0}{w(z)} \exp\left(-\frac{\varrho^2}{w^2(z)}\right) \exp\left(-ikz - ik\frac{\varrho^2}{2R(z)} + i\zeta(z)\right) \tag{2.41}$$

with beam waist

$$w(z) = w_0\sqrt{1 + \left(\frac{z}{z_0}\right)^2}, \tag{2.42}$$

the wavefront radius of curvature

$$R(z) = z\left(1 + \left(\frac{z_0}{z}\right)^2\right), \tag{2.43}$$

the Gouy phase

$$\zeta(z) = \arctan\left(\frac{z}{z_0}\right), \tag{2.44}$$

and the waist at the focus

$$w_0 = \sqrt{\frac{\lambda z_0}{\pi}}. \tag{2.45}$$

The double of the waist is known as the spot size of the beam. The wavelength is described by λ, the direction of propagation is z with

$$z_0 = \frac{\pi\omega_0^2}{\lambda} \tag{2.46}$$

the Rayleigh range and $\varrho^2 = x^2 + y^2$ the distance squared perpendicular to the optical axis. The Rayleigh range is defined as the distance from the focus, at which the cross section of the beam is doubled. Therefore, at the distance z_0 away from the focus, the beam has a size increased by factor $\sqrt{2}$ and an intensity at the optical axis halved with respact to the intensity at the focus.
When going far away from the focus, the laser beam diverges almost linear, since the 1 under the square root in eq. 2.42 can be omitted. If now a collimated laser beam is focussed down by a lens, the focus can be seen as a point source in comparison with the lens diameter D. Using those two approximations, the angular width θ_{tot} of the diverging beam can be approximated by

$$\theta_{tot} \approx \tan(\theta_{tot}) = \frac{D}{f} \tag{2.47}$$

using the approximation $\tan(\theta_{tot}) = \theta_{tot}$ for small angles θ_{tot}. Considering the same geometrical argument of small angles, the angular width near the focus can be expressed as

$$\theta_{tot} = 2\frac{w_0}{z_0} = \frac{2\lambda}{\pi w_0} \tag{2.48}$$

Equating eq. 2.47 and eq. 2.48 leads to

$$w_0 = \frac{2f\lambda}{\pi D} \tag{2.49}$$

meaning the waist and therefore the spot size of the beam is the smaller the bigger the incoming beam diameter on the focussing lens is.
As seen in the section before, off-resonant excitation is proportional to the square of the electrical field. For laser beams, this corresponds to the intensity of the laser beam. Considering again a Gaussian shape, the intensity $I(\varrho, z)$ can be expressed as the absolute square of the Gaussian beam

$$I(\varrho, z) = |U(\varrho, z)|^2 = I_0 \left(\frac{\omega_0}{\omega(z)}\right)^2 e^{-\frac{2\varrho^2}{\omega^2(z)}} \tag{2.50}$$

with $I_0 = |A_0|^2$.

2.5. Quantum simulation

In one of his famous talks in 1981, Richard Feynman [4] proposed using a computer on the basis of quantum mechanics instead of a computer on the basis of classical mechanics to simulate and solve problems in quantum physics. Since the Hilbert [35] space grows exponentially with the number of particles in the problem, the time a classical computer needs to solve such a problem also grows exponentially. In the following years, works like the 1996 paper of Seth Lloyd [36] paved the way for the modern research in the field of (digital) quantum simulation.

One can distinguish two different types of quantum simulation [37, 38]: analogue and digital quantum simulation. In the analogue case, the desired Hamiltonian is directly prepared on the available system and the reaction of the system is studied. In the digital case, the Hamiltonian is prepared and simulated with the help of quantum gates, which allows to simulate basically any Hamiltonian, if the size of the system is large enough. For both types, the quantum simulator can be used not to simulate the total Hamiltonian, but more as a co-processor [39], which simulates only a few properties of the Hamiltonian the classical computer is overburdened with.

2.5.1. Basics

In classical informatics, the bit is the basic unit of information. It can take the values of 0 or 1, True or False, encoding every piece of communication, calculation and information. When talking about quantum bits, qubits, one has basically also a system with two different levels, which can be measured to be either in one or the other state, the ground state $|g\rangle$ or excited state $|e\rangle$. The main difference is, that the qubit can also be in a superposition state $|\psi\rangle$ of the two states [26]

$$|\psi\rangle = c_g|g\rangle + c_e|e\rangle \tag{2.51}$$

where $|c_g|^2 + |c_e|^2 = 1$ has to be fulfilled due to normalization. When measuring the state of a qubit in a single measurement, the result has to be the qubit being either in $|g\rangle$ or $|e\rangle$. Also, c_g and c_e are complex in general, where a classical measurement can only give one the probabilities $|c_g|^2$ resp. $|c_e|^2$. Therefore, one has to make a number of measurements to be able to do statistics and determine $|c_g|^2$ and $|c_e|^2$. The error that is made when determining the probabilities p is the so-called quantum projection noise [40]

$$\Delta p = \sqrt{\frac{p(1-p)}{N}} \tag{2.52}$$

where N is the number of measurements made. In the future discussions, the quantum projection noise will be calculated as

$$\Delta p = \frac{1}{\sqrt{N}} \tag{2.53}$$

which corresponds to the error of a Poissonian process, containing all kind of projection and detection errors and allowing for a more equal weighting of the data points than eq. 2.52. The most correct method would be doing a so called jackknife [41] for each data point. This method works by first taking the mean value $\bar{x}$ of a set of data values $\{x\}$ and then calculating the deviation of the mean value with one data point missing $\bar{x}_i$ relative to the mean of the total dataset. The resulting error can be calculated via

$$\Delta p = \sqrt{\frac{N}{N-1}\sum_i \left(\bar{x}_i - \bar{x}\right)^2} \tag{2.54}$$

A useful means of visualizing the state of the qubit is the so-called Bloch sphere. The poles of the sphere correspond to $|g\rangle$ and $|e\rangle$, whereas all the other, impure states are located in between. A picture of the Bloch sphere is shown in fig. 2.7.

Making use of the angles ϕ of its projection relative to the x-axis and of the angle θ

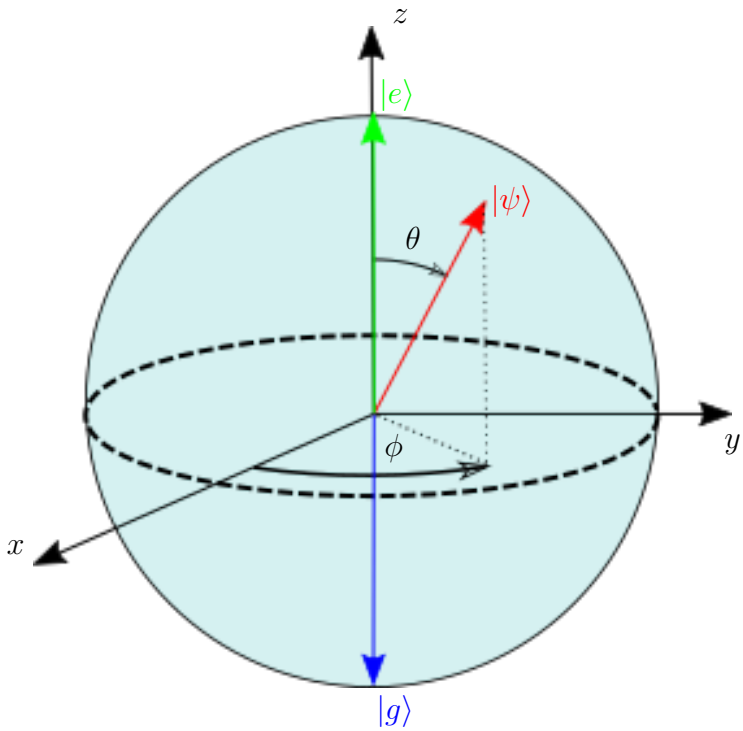

Figure 2.7.: Bloch sphere. The ground and excited state $|g\rangle$ and $|e\rangle$ are located on the poles along the z-axis of the sphere. A general state $|\psi\rangle$ is determined via the angle ϕ of its projection on the x-y-plane relative to the x-axis and the angle θ relative to the z-axis.

relative to the z-axis, the state $|\psi\rangle$ can be expressed as [26]

$$|\psi\rangle = e^{i\gamma}\left(\cos\left(\frac{\theta}{2}\right)|e\rangle + e^{i\phi}\sin\left(\frac{\theta}{2}\right)|g\rangle\right) \tag{2.55}$$

with γ a global phase.

When manipulating the state of a qubit, a rotation along the Bloch sphere is executed. The rotation can be expressed by making use of the Pauli matrices σ_x, σ_y and σ_z defined as

$$\sigma_x = \begin{pmatrix} 0 & 1 \\ 1 & 0 \end{pmatrix} \qquad \sigma_y = \begin{pmatrix} 0 & -i \\ i & 0 \end{pmatrix} \qquad \sigma_z = \begin{pmatrix} 1 & 0 \\ 0 & -1 \end{pmatrix} \tag{2.56}$$

along with the identity matrix. In the experiment, one can basically go everywhere on the Bloch sphere by using suitable laser pulses for changing the state of the qubit. E.g., when exciting the qubit by shooting at it with a laser at resonant frequency, one performs a rotation from pole to pole. Resonant rotations $R_\phi(\theta)$ can be expressed as

$$R_\phi(\theta) = e^{-i\theta S_\phi/2} \tag{2.57}$$

with $S_\phi = \sum_{i=0}^{N} \left(\sigma_x^{(i)} \cos(\phi) + \sigma_y^{(i)} \sin(\phi) \right)$ the sum over all Pauli matrices acting on ion i with N the number of qubits. When the time the laser is exciting the qubit is just right to bring it from one pole to the other, the operation is called a π pulse. Correspondingly, the rotation from one pole to the x-y-plane is called a $\frac{\pi}{2}$ pulse.
Applying off-resonant light causes the vector of the state to rotate along the z-axis [42]. Here the rotation is not dependent on the phase of the laser, meaning AC-Stark shifted light is suitable for this type of operation. The operation $S_z^{(j)}(\theta)$ on the jth qubit can be expressed as

$$S_z^{(j)}(\theta) = e^{-i\theta\sigma_z/2} \tag{2.58}$$

with the angle $\theta = \delta_{AC} t$ dependent on the AC-Stark shift eq. 2.32.

3. Addressing setup

In the IQOQI's trapped-ion quantum simulation experiment, the quantum state is prepared rotating the state of each individual qubit in the corresponding state using a tightly focussed laser beam. In order to be able to prepare the state of each ion, the focal spot has to be movable over the whole ion string. Before the beginning of the work for this master thesis, the ions were addressed using an optical setup built by Ben Lanyon, which was actually designed to address a few ions and limited to the addressing of 20 ions, corresponding to an addressing range of about 100 µm. A scheme of this setup can be found in fig. 3.1. It basically consisted of an AOD, in which the laser beam was coupled, and a Galilean beam expander. The main problem was, that out of a certain frequency range, the laser beam started clipping on the objective, leading to less or no laser power at all being led to the ions. The main task of this thesis was to come up with an optical setup, which allows for the addressing of 50 ions, which corresponds to an addressing range of roughly 230 µm due to technical constraints.

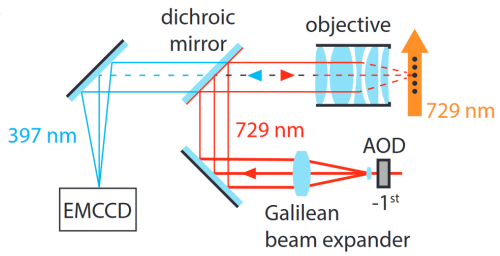

Figure 3.1.: Old addressing setup. A laser beam is coupled into an AOD and expanded using a Galilean beam expander. The beam is guided to the upper level of the setup by a common and a dichroic mirror and then focussed to the ion string using a custom made objective. This objective is also used for imaging purposes. The picture was taken from [26].

In this chapter I will first motivate why an AOD is the right choice to steer a beam over an ion string, then present the simulations made and the setup constructed to solve the presented problem along with data gathered from a test setup and the characterization of the AOD.

3.1. AODs

When it comes to the deflection of laser beams, the use of non-linear effects in optical crystals is a commonly used technique. These effects can be caused for example by electrical fields, as it is the case for electro-optical modulators, or by acoustic waves, as it is the case for acousto-optical modulators and deflectors. In the latter case, by changing the index of diffraction periodically, a sinusoidal grating is generated in the crystal, leading to the diffraction of an incoming laser beam into several orders. In another picture, the momentum of the acoustic phonon of frequency Ω_{RF} is absorbed

by the incoming photon of frequency ν, resulting in an exiting photon with different direction and frequency $\nu + \Omega_{RF}$.
The diffraction angle θ is dependent on the velocity of sound of the material v via

$$\theta = \frac{\lambda \Omega_{RF}}{v} \tag{3.1}$$

with λ the wavelength of the input laser beam. The main difference between an AOD and an AOM is that the material AODs are made of have a far lower velocity of sound compared to the one AOMs are made of, leading to a bigger diffraction angle. Therefore, AODs are the first choice whenever a beam has to be steared over a large angle.
The downside of a small velocity of sound is, that the time the sound wave needs to reach the laser beam in the crystal is bigger in comparison to an AOM, which means the laser beam can't be steered with an AOD as fast as with an AOM.
Besides the difference in the material, i.e. velocity of sound, the working principle of an AOD and an AOM are the same.

3.2. Simulation

The first step of designing a new setup are always simulations. For this purpose, the software ZEMAX was used, which allows for simulating a system using not only ray optics, but also Gaussian beam propagation. This enables the designer to see where on the beam path optical aberrations arise and how to fix them. Also, for most lenses available from manufacturer side, ZEMAX lens files exist, which makes it quite easy to insert a certain lens into the simulation.
The simulations made for this thesis were based on an approach made by Christoph Steinlechner, the master student working on the project before myself. It consisted of five lenses, where two of them were stock lenses, and had a total length of roughly 80 cm. The working principle of his setup is very similar to mine, whereby the total length of the setup was reduced to match the available roughly 60 cm of linear beam path. Also, all the lenses were selected to be stock lenses, which reduced cost and shipping time, but not the performance of the setup.

3.2.1. ZEMAX software

When opening ZEMAX for the first time, the 'Lens Data' tab opens automatically. In this tab, one can either define ones own lenses or load already existing lens files, e.g. ones provided by the manufacturers. A variety of characteristics of the lens can be determined, such as radius of curvature, thickness, material and coating. If not specifically put somewhere else, all the optical components are centred around the optical axis of the system.
A very useful tool of the software is the '3D Layout' tab. Here, the optical system can be viewed as a 3D model, whereby ray optics is used to calculate the paths of

the displayed rays. That way, clipping effects can be seen already in this model. A screenshot of this tool is shown in fig. 3.2. The rays can be defined at the 'Fields'

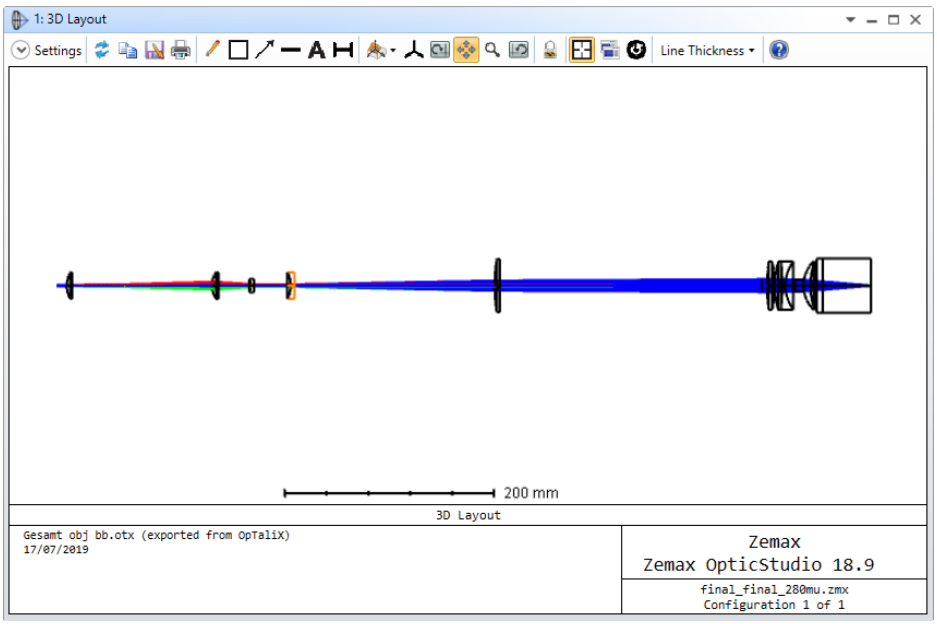

Figure 3.2.: Screenshot of the '3D Layout' tab in the ZEMAX software. The lenses of the setup are centred around the optical axis of the system, the distance between them can be changed in the 'Lens Data' tab. The rays coming out of the object plane span an angle of 2.7°, as the output range of the AOD is specified. The center ray is coloured in blue, the two rays at the edges of the range are coloured in red and green. The surface marked in orange is the one selected in the 'Lens Data' tab.

option in the 'System Explorer' tab. This option was used to define three beams at the edges and the center of the angular output range of the AOD. When looking at the edge beams at the focal plane in the '3D Layout' tab, one can measure the achievable addressing range. What one may notice looking at fig. 3.2 is, that the third lens from the left (labelled L3 in fig. 3.5) is different from the one specified in section 3.3. This is due to the fact, that the simulations were made using a 1/2 inch lens, which was changed to a 1 inch lens when mounting the setup into the experiment due to clipping and accuracy concerns. The optical properties (focal length) of the lens in the actual setup are the same as the ones of the lens in the simulations.
The third very useful tab was the 'Physical Optics Propagation' tab, which calculates the beam profile at a desired surface along the beam path using scalar diffraction theory. Hereby, the wavefronts are propagated through the setup using transfer functions on an array of sampled points [43], whereby the user can choose the amount of points and thereby the resolution of the simulation. Using this functionality, one is able to take a look at the beam and its profile also close to and at the focus of the beam, where ray optics breaks down. Also, optical aberrations are calculated more precisely and are visualized better than for the ray optics. A picture of the beam profile at the focus is shown in fig. 3.3.

A very useful tool when doing simulations was the 'Quick Adjust' Option in the

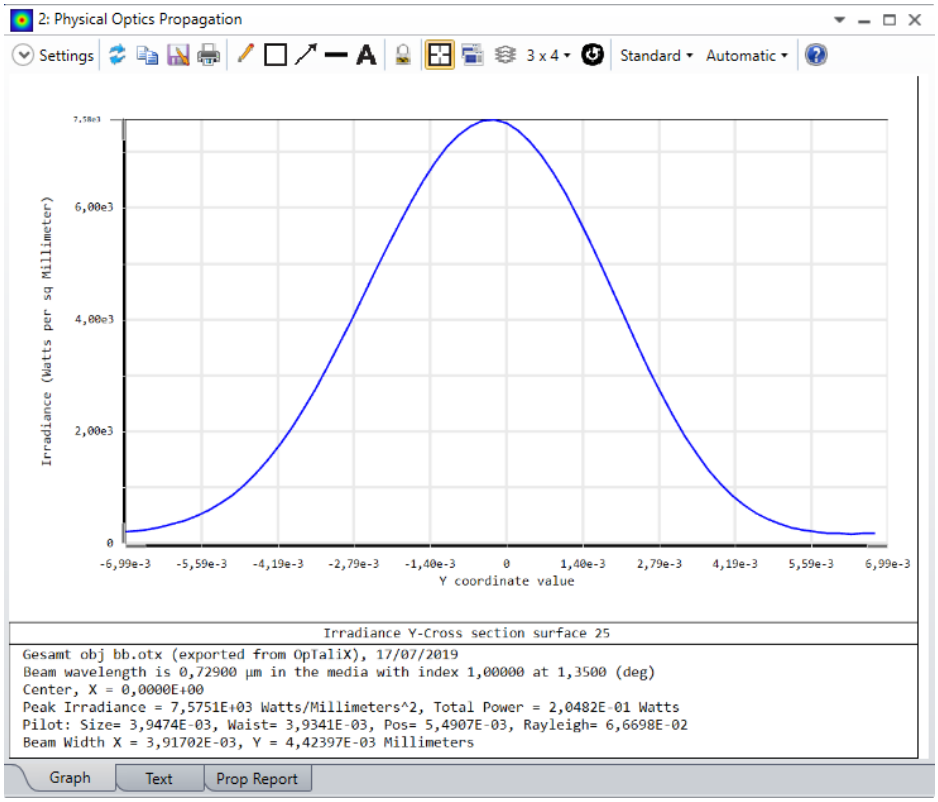

Figure 3.3.: Screenshot of the 'Physical Optics Propagation' tab. In the plot, the irradiance is plotted as a function of the spatial expansion of the beam.

'Optimization' menu. This allows the optimization of a certain distance between two surfaces or the radius of curvature of a surface in the setup, in order to get the focus at the image plane.
Of course, the possibilities in ZEMAX are much larger than the ones quickly presented above, but as a start, those options turned out to be quite useful.

3.2.2. Simulation results

From the simulation, a spot size of the beam of 2.4 µm was obtained for an addressing range of 200 µm. This waist was slightly larger than the spot size obtained in the old setup, which was about 2.0 µm. The differences can be explained with the larger addressing range, since the spot size and the addressing range are correlated. At the same time, concerns arose, whether the objective in the simulation really represented the one actually built into the experiment. This was the case, since in the simulation it was not possible to reach diffraction limited spot sizes as specified in [26]. On the other hand, the focal length of the objective matched with the distance from the last lens of the objective to the ions of 5.8 cm, as specified in [44].
The only option to reach spot sizes in that region is to increase the beam size entering

the objective, resulting in a smaller spot in the focus. But this can't be simply be achieved by expanding the beam more, since this would at the same time decrease the addressing range, but rather by increasing the beam size going through the AOD, i.e. using a fibre coupler with a bigger output diameter and an AOD with a bigger aperture. Doing this, one has to take into account the larger response time due to the larger distance the sound wave has to walk until the whole laser beam is deflected. Also, the risk of optical aberration rises, since the diffraction of the lenses gets more and more imperfect the further one moves out of the center.
Simulated results for both effects, which were described in the paragraphs above, can be found in fig. 3.4.

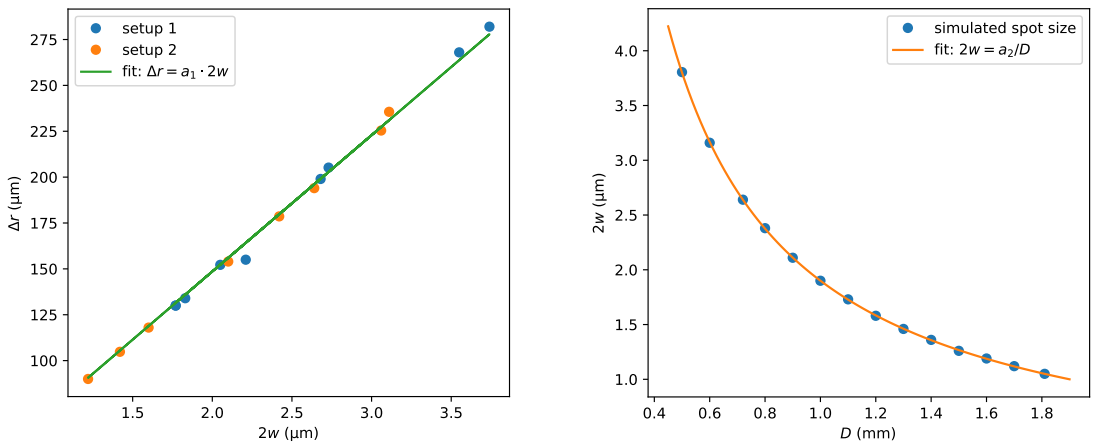

(a) **(b)**

Figure 3.4.: Correlations important for the simulations: in (a), the addressing range Δr is plotted as a function of the spot size at the focus $2w$. The calculations were made for two different lens configurations to make sure the limitation is not coming from a specific design. There was also made a linear fit $\Delta r = a_1 \cdot 2w$ in order to show the observed linear correlation. The parameter a_1 was found to be $a_1 = 74.3(1)$, where the error comes from the fit error. In (b), the spot size of the laser beam at the focus is plotted as function of the input diameter D of the laser beam at the AOD. Also here, a fit was made as expected by eq. 2.49 of the form $2w = a_2/D$, where a_2 was found to be $a_2 = 1.90$ with negligible error arising from the fitting. In both cases, the values didn't have errors, since ZEMAX doesn't give errors on its output values.

3.3. Setup

In this section, the developed setup and its specifications are presented. The setup consists of the AOD, 5 lenses and the objective. There are additional components like a polarizing beam splitter and mirrors, which are also part of the setup, but are not important for the main task of the setup, which is allowing us the precise addressing

of single ions spaced over a certain distance range from the optical axis. A sketch of the setup can be seen in fig. 3.5, where a few (not all, for a better overview) of these additional components can also be seen.

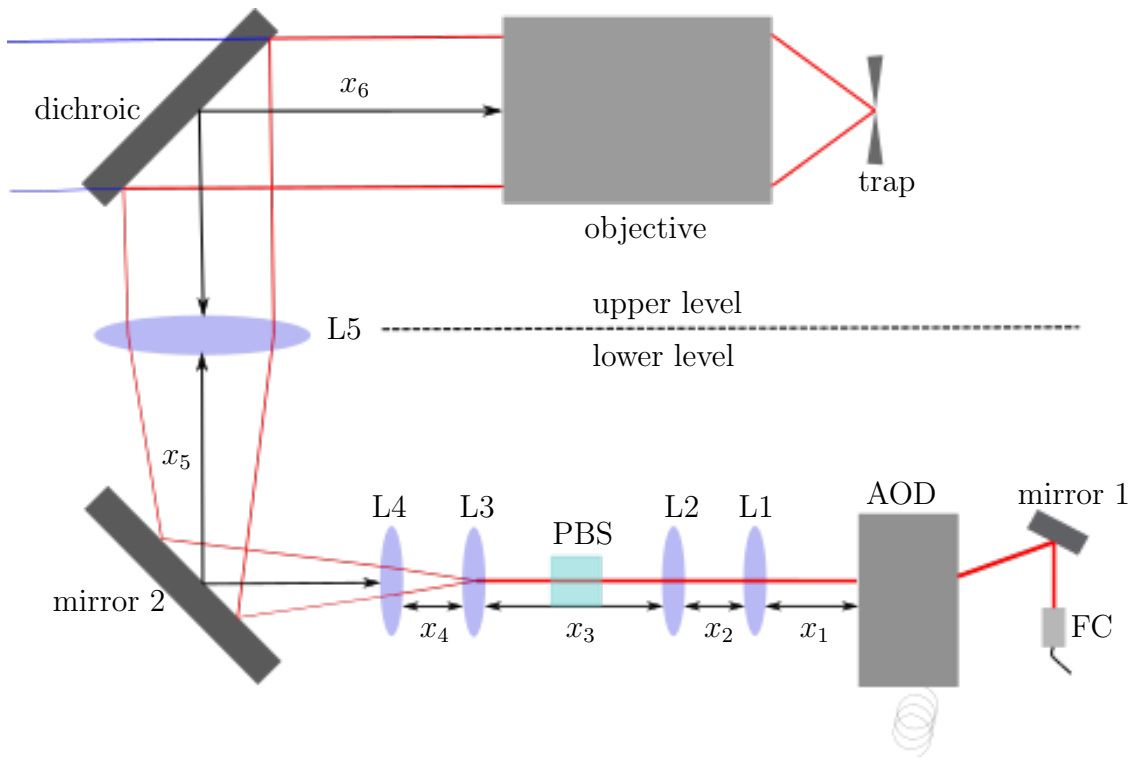

Figure 3.5.: Sketch of the setup. The 5 lenses in the setup are described with L1...L5, whereby L5 can be moved in x,y and z with piezo actuators. The distances between the lenses (surface to surface) are described with $x_{1,\ldots,6}$. PBS denotes a polarizing beam splitter, AOD the acousto-optical deflector and FC the fibre coupler.

The 729 nm laser light is coupled from a polarization maintaining fibre with a Schäfter + Kirchhoff A8 fibre collimator [45] and directed with a 1 inch mirror (mirror 1) to the aperture of the AOD. These components, the lenses L1 to L4, a polarizing beam splitter and the mirror directing the beam to the upper level of the setup (mirror 2) are located below the vacuum chamber. Besides the mirrors, the fibre coupler, a polariser and a $\lambda/2$ plate, both located between fibre coupler and mirror 1, all components are mounted on a breadbord, custom made by the mechanical workshop of the IQOQI. This allows the positioning and aligning of the components without having to crawl underneath the vacuum chamber. The purposes of the additional components like the $\lambda/2$ plate and the PBS are the aligning of the polarization of the laser light and the filtering of unwanted back-reflected light.
Lens L5 is located between the two levels and can be moved in x, y and z direction in order to get the focus of the laser beam to the right position of the ion chain in the trap. This is achieved using Newport piezo actuators [46]. Between L2 and L3,

Table 3.1.: Porperties of the lenses used in the setup. The abbreviation 'foc.l.' stands for the focal length, 'dia.' for the diameter and 'th.' for the thickness. The thickness is hereby the center thickness.

lens	part number	foc.l. (mm)	dia. (inch)	th. (mm)	material	manufacturer
L1	LA1131-B	50.0	1	5.3	N-BK7	Thorlabs
L2	LA1422-B	40.0	1	6.4	N-BK7	Thorlabs
L3	KPC043AR.16	-25.0	1	2.5	N-BK7	Newport
L4	LC1715-B	-50.0	1	3.5	N-BK7	Thorlabs
L5	LA1256-B	300.0	2	5.1	N-BK7	Thorlabs

Table 3.2.: Spatial distances in the setup.

distance	value (mm)
x_1	10.0
x_2	122.5
x_3	31.0
x_4	35.0
x_5	191.2
x_6	250.0

there is a cubic polarizing beam splitter with a diameter of 1.5 cm. The lenses L3 and L4 act as a Galileian beam expander, together with the collimating lens L5. There were two lenses used for the expansion, since there was no single suitable stock lens available. The lenses L1 and L2 are there in order to project the output of the AOD on the objective, which means that by changing the drive frequency of the AOD, the expanded laser beam always hits the same area of the input lens of the objective (and more or less also of the collimating lens). In the old setup, clipping of the beam on the collimating lens was a major problem limiting the addressability of more than 20 ions.
The objective and the vacuum vessel are located on the upper level. The light is guided there via two 3-inch mirrors, one of which is mounted on the lower level and the other on the upper one. The mirror on the top level is a dichroic mirror, which means that it acts as reflector for light in a certain wavelength range and as transmitter for light in another range. This is necessary, since the objective is also used for imaging purposes and therefore transmits the 397 nm light emitted by the ions when driven on the $4^2\mathrm{S}_{1/2} - 4^2\mathrm{P}_{1/2}$ transition.
The objective is located inside a reentrant viewport. With this arrangement, the last lens of the objective is only roughly 6 cm away from the ion without the need of putting the objective inside the vacuum system.
In table 3.1, one can find the specifications of the lenses. All the lenses are anti-reflectance-coated for 729 nm light. The reflectance is lower than 0.5 % for both the Thorlabs and Newport lenses [47, 48]. This helps preventing noise on the ions caused by reflected beams.

In table 3.2 the surface-to-surface distances $x_{1,\dots,6}$ between the surfaces of the lenses are listed. The distances are always given as the distance from the center of the surface to the next one. The simulations showed, that the setup is most sensitive to changes of x_3 and x_5, whereas variations of $1-2\,\mathrm{mm}$ of x_1, x_2, x_4 and of $1-2\,\mathrm{cm}$ of x_6 don't change the properties of a setup drastically. Any changes of the focal length of the total system within the latter variations can be compensated by changing x_5 with the piezo actuators.
An important point is also the placing of the beam splitter in the optical path. With an edge length of $d = 1.5\,\mathrm{cm}$ and a refractive index of $n_{cube} = 1.7$, the effective optical pathlength within the cube is $d \cdot n_{cube} = 2.55\,\mathrm{cm}$. So the pathlength is 1.05 cm longer with cube than without. This circumstance was taken into account for the distance x_2 in table 3.2, since the simulations were made without a beam splitter in the optical path.

3.4. Characterization of the AOD

The main component of the optical setup, besides the lens configuration, is the AOD. An AOD can deflect a laser beam by giving the photons an additional momentum, using a sound wave in a crystal. This momentum also shifts the laser frequency by the corresponding value, which can either be compensated via two upstream AOMs or used for off-resonant addressing.

3.4.1. Diffraction efficiency

For the purpose of addressing a 50 ion string with roughly 2 µm spot size, it is crucial to have a rather big angular range. With the AOD used, an angular range of 2.7° can be scanned using a frequency range from 60 MHz to 100 MHz as specified by the manufacturer (ISOMET, see appendix B). For the addressing, the ions have to be exposed to a certain power for a certain time, where as a rule of thumb "the more power the better" is valid. Therefore, during the scanning as little power as possible should be lost to the 0th diffracted order as well as higher orders than the 1st order of the AOD.
The AOD is placed in such a way, that the incident beam hits it at the Bragg angle of the TeO_2 crystal inside, which is about 2.7°. The center frequency of the AOD is 80 MHz, the frequency with highest diffraction efficiency, i.a. the amount of power in the 1st order diffracted beam in relation to the total transmitted power, is at about 85 MHz. A comparison with the diffraction efficiency specified by ISOMET and the measured one is shown in fig. 3.6.
As one can see, the diffraction efficiencies match quite well, small differences of the location of the drive frequency with the largest diffraction efficiency can be explained with slightly different optimization angles, since the measured curve was optimized at the center frequency of 80 MHz.

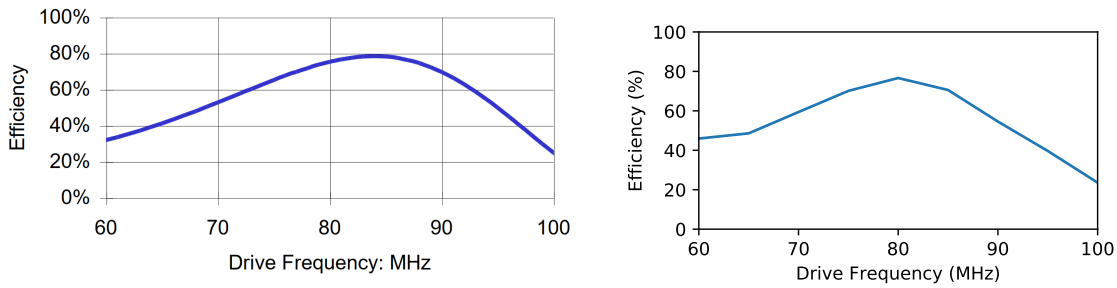

(a) Diffraction efficiency as specified by ISOMET

(b) Measured diffraction efficiency

Figure 3.6.: Comparison between specified (a) and measured (b) diffraction efficiency

3.4.2. Power dependence

The diffraction efficiency of the AOD is not only dependent on the applied drive frequency, but also on the applied RF power. The bigger the RF power, the better the diffraction works, but only up to a certain limit, where the RF power becomes so high, that it can actually damage the crystal. Therefore one would like to work at the upper bond of the recommended RF power of <1 W (see appendix B). The rising diffraction efficiency can also be seen in fig. 3.7.

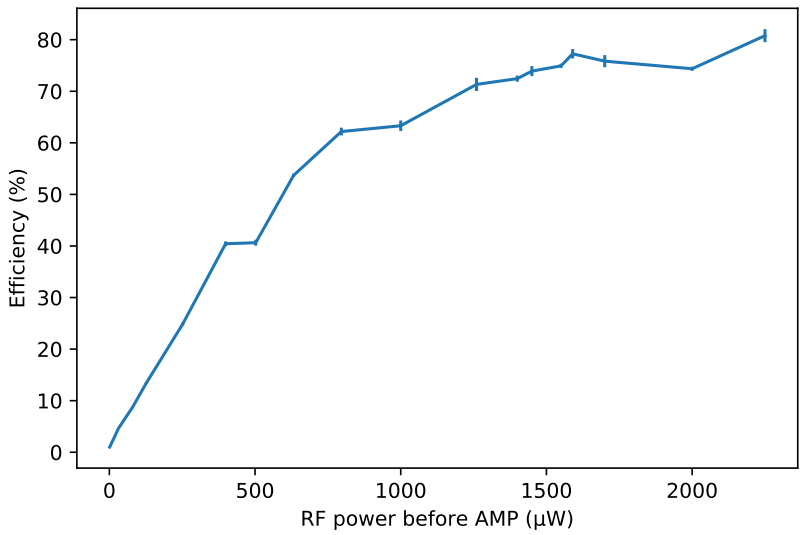

Figure 3.7.: Diffraction efficiency as a function of the applied RF power at the AOD. The RF power was measured before the amplifier, which provides an amplification of 29 dB [49]. The errors are due to fluctuations in the measured laser power.

The amplifier has a gain of 29 dB [49], which means that for an input of 1.25 mW, the threshold of 1 W output is reached. At about this point, the diffraction efficiency seems to saturate, which can be explained by the saturating amplifier.

3.4.3. Response time

Another very important property of the AOD is the time it takes, to move the beam spot from one place to another one in the ion string. This time is the so called response time, whose measurement is shown in fig. 3.8. The total time from the rise of the RF signal until 90 % of the laser power is deflected is 4.6 µs, whereas the time for the rise of the deflected power from 10 % to 90 % is 2.0 µs and the time from the RF signal until the photodiode signal starts rising is 2.3 µs. The laser beam input into the AOD was adjusted in such a way, that it is closest to the RF source in the AOD in order to decrease the time required for the sound wave to reach the laser beam. This time is suitable for doing addressing of multiple ions for quantum simulation purposes. A fast photodiode with a bandwith of 25 MHz was used for this measurement.

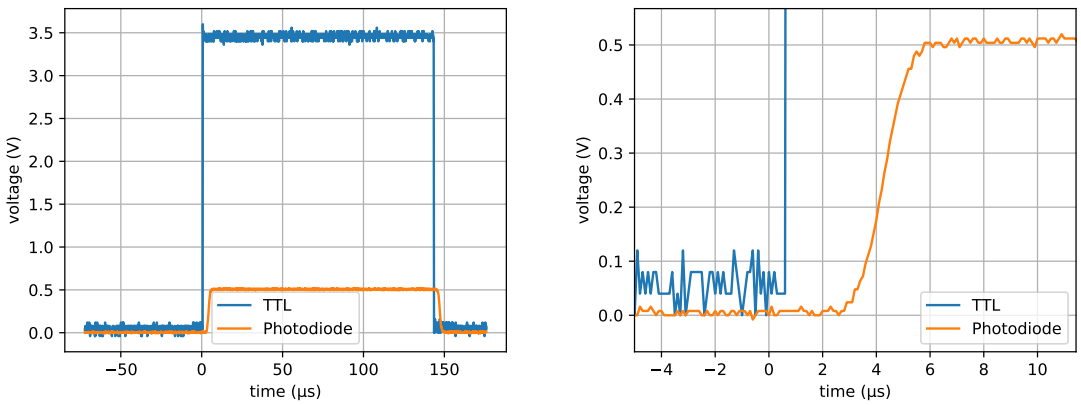

(a) (b)

Figure 3.8.: TTL signal triggering the RF power and photodiode signal measuring the output of the AOD in the first diffraction order as a function of time. The left panel (a) shows the response of the AOD to a rectangular rf-pulse; the right panel (b) shows the rise of the optical power on a smaller time scale. The time the photodiode signal needs to rise from 10 % to 90 % is 2.0 µs. The time from the triggering until the photodiode signal starts rising is roughly 2.3 µs.

3.5. Test setup

In order to make sure that all the properties of the setup behave as expected from the simulations, a test setup was built and some properties like the beam profile, multiple frequency input and - most importantly - the addressing range and the spot size determined. The results are described in the following paragraphs.

3.5.1. Beam profile

Since there are non-linear effects going on in the AOD, it's not clear from the beginning, that the shape of the deflected beam matches the shape of the input beam. Fig. 3.9 shows the beam profile after its path through the AOD, all the lenses and the objective. The picture was taken far away from the focus in order to see possible non-Gaussian shapes better. One can say, that the shape of the beam is still radial symmetric, which also means that there are no major aberrations caused by the lenses or clipping of the laser beam.

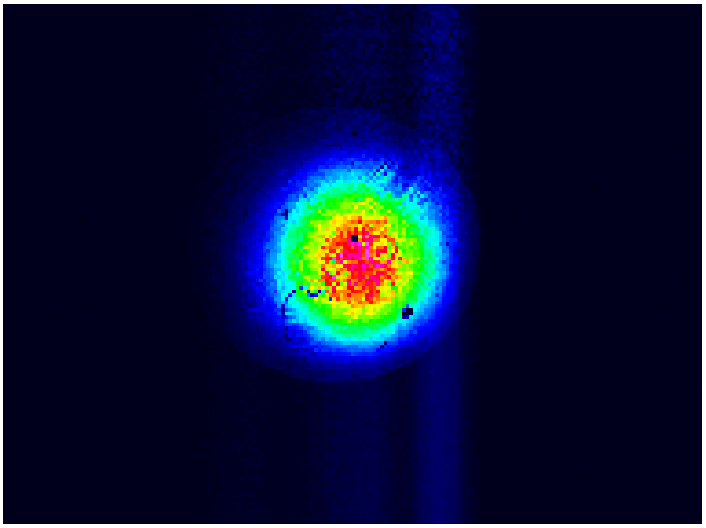

Figure 3.9.: Beam profile of the deflected laser beam after running through all the lenses and the objective. The picture was taken far away from the focus.

3.5.2. Spot size

A quite time-demanding activity during this thesis was the determination of the spot size of the laser beam in the focal plane. The first attempt to measure it was by doing knife-edge scans, using a razor blade mounted on a translation stage, moved by a piezo actuator with a step size of 10 nm. For a laser coupler that provided an output beam diameter of 1.44 mm, the simulation predicted spot sizes of about 2.4 µm, but the best result obtained by these scans was 3 µm. In these measurements the spot size was determined by fitting the data gained from taking the voltage of the photodiode after every step of the piezo actuator. An exemplary dataset with fit is displayed in fig. 3.10. Here an error function was used as fit function, since for a Gaussian beam the signal recorded by the photodiode is the integral of a Gaussian intensity function. In the example, the spot size is roughly 18 µm. This measurement was not taken in the focus, but was chosen to be displayed, since the shape of the error function can be seen better compared to a dataset, where there is almost just a step function visible.

The reason for the broader than expected spot size are thought to be vibrations of

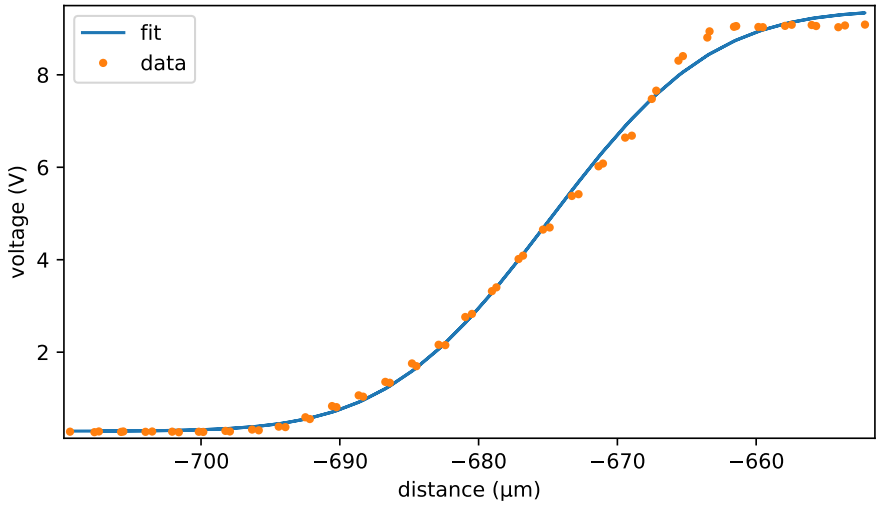

Figure 3.10.: Exemplary data set of a razor blade scan. The voltage at the photodiode is plotted as a function of the travelled distance of the piezo actuator. The data was fitted with an errorfunction, which corresponds to an integrated Gaussian.

the razor blade, caused by the piezo steps, which leads to a broadening of the beam in the focus.
A second approach was made using a CCD camera with a pixel size of 1.67 µm. The camera was placed on a translational stage and moved to the focal plane. The laser beam had to be attenuated in order not to saturate or destroy the camera. Here a gradient attenuator turned out to be quite useful, with whom the power at the CCD could be adjusted quite precisely to the required value. A two-dimensional fit was made in order to determine the spot size of the laser beam at the focal plane using a Mathematica script adapted from a script written by Manoj Joshi. Also, the spot sizes of the beam were determined when moving it out of the focus. By theory, the spot size should be twice the size of the waist as given in eq. 2.42 . Measurements were taken by displacing the CCD camera in steps of 40 µm by using a micrometer screw. The result is shown in fig. 3.11

One can see from the figure, that fit and measured value do not match quite well in the focus. The reason for that is, that for this small values of the waist, the Gaussian in one direction perpendicular to the optical axis is only defined via a few points. Simulations comparing a Gaussian with a Gaussian reconstructed with three points gained out of its integral show, that the real Gaussian has a waist up to 10 % smaller than the reconstructed one. When taking this into consideration, the measured and fitted waist match quite well. In fig. 3.12 one can see a fit done with Mathematica.

Th fits were made using a fit function similar to eq. 2.50, namely

$$I(x,y) = A \cdot \exp\left(-\frac{(x-x_0)^2}{2w_x^2} - \frac{(y-y_0)^2}{2w_y^2}\right) + C_o \tag{3.2}$$

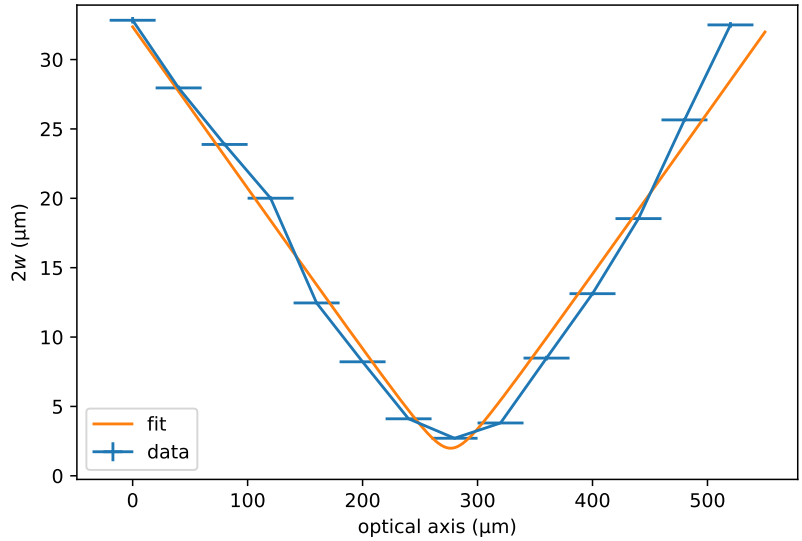

Figure 3.11.: Spot sizes $2w$ of the laser along the optical axis around the focus. The minimum measured value is 2.4 µm, the fitted minimum spot size is 2.0 µm, where the errors of both values are negligible. The error bars regarding the optical axis are due to uncertainties when moving the micrometer screw, the error bars regarding the spot size are the errors obtained when fitting the camera data and can barely be seen. The fit was made without consideration of the errors regarding the optical axis.

where I describes the intensity of the laser beam, x_0 and y_0 the position of the beam on the CCD, w_x and w_y the waist of the beam in the plane of the CCD and C_o a constant offset caused by background stray light and noise of the CCD. To get the effective spot sizes, one has to multiply w_x and w_y with $2 \cdot 1.67\,\mu\text{m} = 3.34\,\mu\text{m}$. The fit function was chosen that way, to account for possible inequalities in the beam size in the two dimensions perpendicular to the optical axis.

3.5.3. Multiple frequency input

When doing quantum simulation, at some point it might be necessary not to address only a single ion at the time, but two or more ions at the same time. In order to quantify second-order effects caused by frequency addition, two different RF-frequencies were combined on a 50/50 power splitter, and the resulting signal was amplified and applied to the AOD. The output of the power splitter was analysed with a spectrum analyser before and after the amplifier, which showed that the second harmonics of both applied frequencies were present in the spectrum with powers on the order of 1 % of the total power. But those double frequencies can be ignored, since for all applicable frequencies to the AOD, they lay out of the used frequency range from 60 MHz to 100 MHz. What cannot be ignored are the difference frequencies of the two applied frequencies respective to their double frequencies. E.g. for applied frequencies

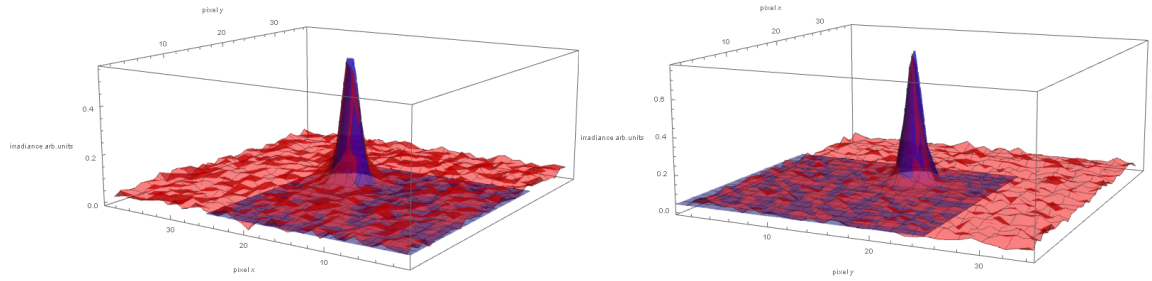

(a) **(b)**

Figure 3.12.: Two examples of the fits done with Mathematica. The red area marks the camera data, the blue data the fit. The axes describe the two pixel directions on the CCD camera.

f_1 and f_2, one receives frequency components of $2 \cdot f_1 - f_2$ and $2 \cdot f_2 - f_1$. Those additional frequencies can also be seen on camera images of the focal plane, see fig. 3.13. The not-so-Gaussian shape of the two central spots is due to saturation effects of the camera. The power of the two spots on the side is on the order of 5 % of the power of the spots in the center and on the order of 2 % of the total power.

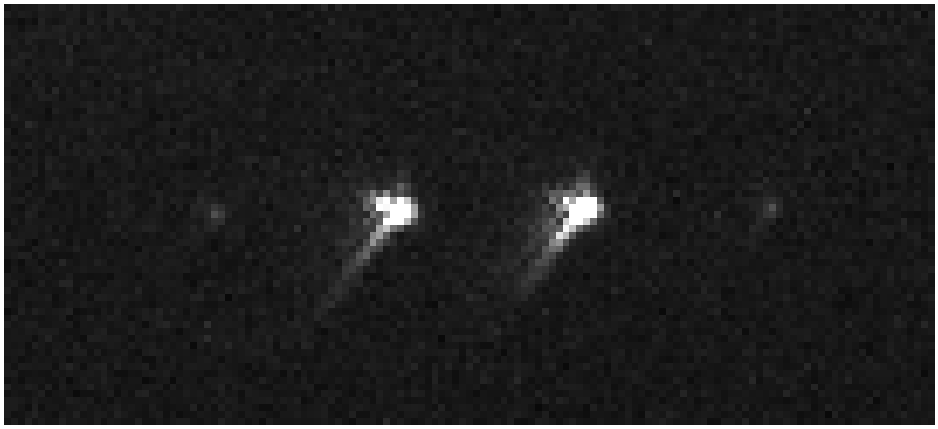

Figure 3.13.: Picture of the focal plane with frequencies (f.l.t.r.) 85, 75, 65 and 55 MHz when applying signals at 65 and 75 MHz simultaneously to the AOD.

3.5.4. Addressing range

The addressing range was determined using again the 1.67 µm pixel-sized camera . Frequencies of 60 and 100 MHz were applied and the pixels between the two appearing spots were counted. The two overlaid pictures are shown in fig. 3.14. The distance between the two visible spots is 119 pixels, corresponding to 199 µm. Here, one of the two main conditions of the whole setup, namely the addressability of a range of 200 µm (the exact value is dependent on the applied trap frequency), is fulfilled.

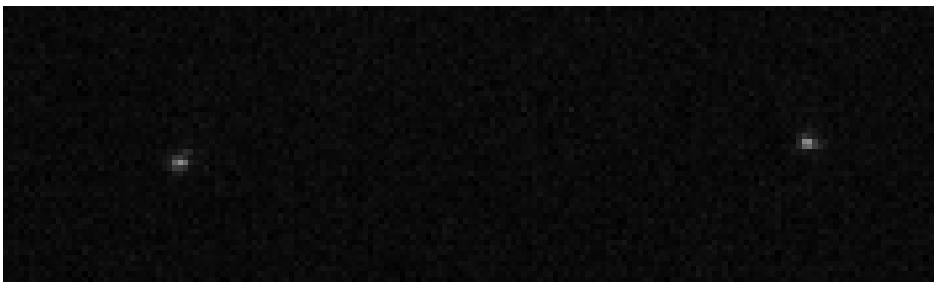

Figure 3.14.: Overlay of two camera pictures with 100 MHz (left spot) and 60 MHz (right spot) applied to the AOD. The distance between the two spots is 119 pixels, corresponding to 199 µm.

3.5.5. Comparison between old and new setup

The value for the spot size of 2.0 µm extracted out of the fit compares well with the value of 2.0 µm measured in the old setup in a resonant frequency scan. For this comparison, it was taken into account, that resonant excitations are proportional to the electric field and not to the intensity (meaning the value was already divided by a factor of $\sqrt{2}$, which connects resonant and off-resonant spot sizes). That way, the new setup has a comparable spot size and a far wider addressing range than the old one, which was about 106 µm for 20 ions.

4. 50 ion addressing

After having characterized the addressing test setup with the measurements described in the previous chapters, the setup was integrated into the trapped-ion quantum simulation experiment. In this section, measurements are described that characterize the addressing setup using the best possible sensors for this purpose, namely ions.

4.1. Building process

The first version of the addressing setup built into the experiment contained a 1/2 inch lens for L3 (see fig. 3.2 and fig. 3.5). The distances $x_{1,\ldots,5}$ (see fig. 3.5) were slightly different and were obtained from the simulation of a 200 µm addressing range. First tests, using the ions in the trap as sensors, revealed, that the spot size was in the right region, but the addressing range was on the order of just 150 µm, allowing for the addressing of only 37 ions.
Also, in the mean time, further discussions revealed, that the addressing range for 50 ions would have to be roughly 230 µm, since otherwise the confinement of the ions in the axial direction would have been too strong. Therefore, new simulations were made, which again resulted in a too small addressing range of 170 µm. By replacing the 1/2 inch lens with a 1 inch lens and doing simulations for a 280 µm addressing range, the addressability of 51 ions was made possible in the end. The parameters $x_{1,\ldots,6}$ of this most recent simulation correspond to the ones listed in table 3.2.

4.2. 51 addressed ions

A plot showing that 51 ions can be addressed individually, made soon after reaching the goal of addressability, is shown in fig. 4.1. For the addressing, an off-resonant laser beam was used to enable AC-Stark addressing (see sec. 2.3.1). The overall shape is due to lower diffraction efficiency of the AOD at the edges of the addressing range. One can also see a noise level affecting all the ions on the order of $2-4\,\%$, which can be explained with high frequency noise in the laser beam, which was only fixed a few months after this measurement was taken. Crosstalk with the neighbouring ion can be excluded as source of the noise, since the noise is there for all the ions and not only for the neighbouring ions of the ion the laser beam is directed at.

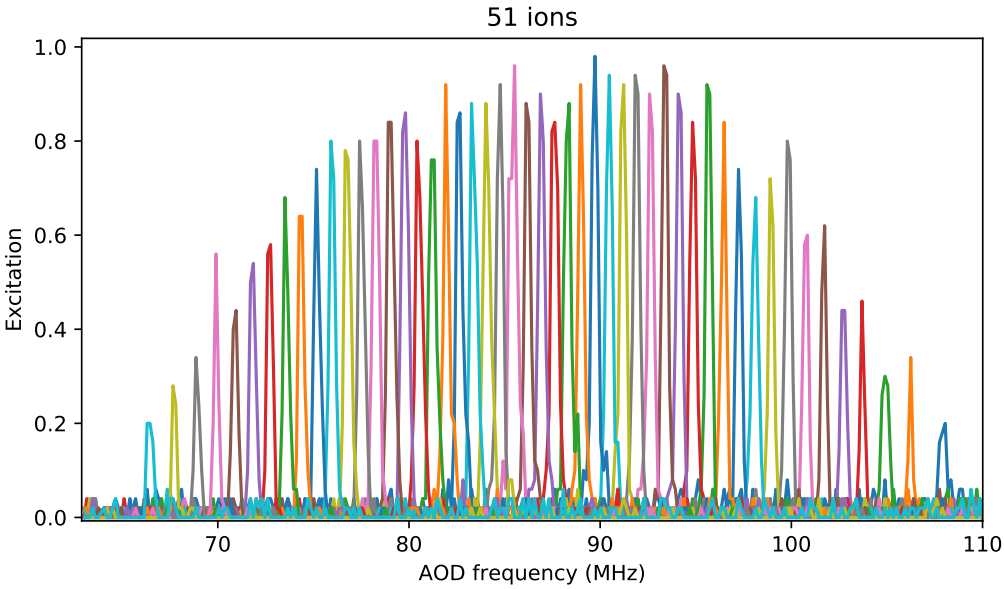

Figure 4.1.: Off-resonant frequency scan obtained by sandwiching an addressed AC-Stark pulse into a global Ramsey excitation (for more details, see main text). The frequency of the AC-Stark pulse was scanned from 63 to 110 MHz. The excitation of the different ions is depicted in different colors, error bars due to quantum projection noise were omitted for better visibility.

4.2.1. Pulse sequence

The sequence usually used for the off-resonant addressing consists of a resonant $\frac{\pi}{2}$ pulse, which brings all the ions from the ground state $|g\rangle$ to the equator of the Bloch sphere. Then there is an off-resonant π pulse shone at a certain AOD frequency, which rotates the state vector around half of the Bloch sphere along the equator (for an ion, which is fully hit by the laser beam). In the end, another resonant $\frac{\pi}{2}$ pulse (the inverse of the first one) is shone on all the ions, bringing the addressed ions to the excited state. A scheme of this sequence is sketched in fig. 4.2.
An ion which is not hit by the off-resonant pulse, is transferred to the ground state $|g\rangle$ by the last resonant pulse. If an ion is only partly hit by the off-resonant pulse, its probability to reach the excited state in the end goes down accordingly. This explains the rising of the excitation, before reaching its maximum, when the ion is fully hit, and then falling again.
Not all the ions reach an excitation of 1. On the wings, this behaviour can be explained by the lower diffraction efficiency of the AOD, meaning that not enough light is diffracted to accomplish a π pulse. When doing quantum simulation, the pulse length required to carry out a π pulse for those ions is changed accordingly, to guarantee equal excitation on the whole ion chain. In the center, the effect of not reaching an excitation of 1 can be explained by the focal spot hitting some ions more precisely than others, which means again a different π time for all the ions. This effect

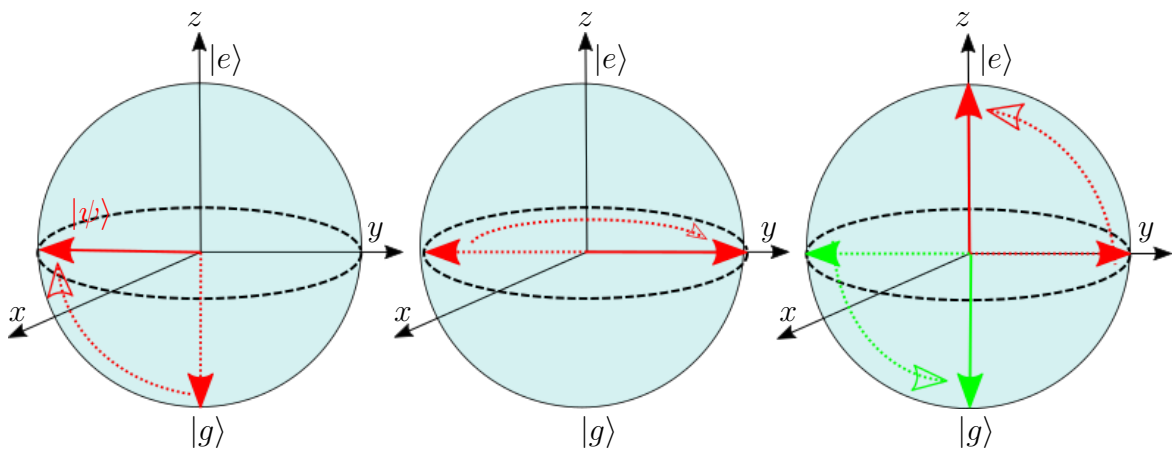

Figure 4.2.: Scheme of the Pulse sequence for off-resonant addressing. The state vector $|\psi\rangle$ of the addressed qubit is depicted in red, the state vector of an unaddressed qubit is depicted in green. With a resonant $\frac{\pi}{2}$ pulse, the state vector is brought from the ground state $|g\rangle$ to the equator (the x-y-plane) of the Bloch sphere. By shining an off-resonant π pulse on the qubit, it evolves 180° around the equator. A qubit, which is not addressed, remains in the same state. A final resonant $\frac{\pi}{2}$ pulse carries out an operation which is the inverse of the operation induced by the first resonant $\frac{\pi}{2}$ pulse, transferring the addressed qubit to the excited state $|e\rangle$ and the unaddressed one to the ground state $|g\rangle$.

plays of course also a role on the wings, but the effect of the lower diffraction efficiency is much more prominent there.
The determination of the π times can be done by first locating the exact position of an ion via a frequency scan and fitting the excitation with a Gaussian, at whose maximum the ion sits. Then a pulse length scan is done, meaning stepwise increasing the pulse duration time of the laser pulse shone on the ion. The result of this are Rabi oscillations. The time when the excitation reaches its maximum the first time, is then the π time. The $\frac{\pi}{2}$ time is naturally half of the π time. Of course, the π times for resonant and off-resonant excitations are different, since their Rabi frequencies are different (see eq. 2.34).

4.3. Focal spot

4.3.1. Beam shape

For the purpose of addressing, it is very important for the beam to have an approximately Gaussian shape. If the shape, due to aberrations, isn't Gaussian, as the beam comes out of the fibre coupler, power is transferred from the centre of the beam profile to its wings, leading to less power being brought on the addressed ion and, in the worst case, to more power being brought to the neighbouring ions, leading to unwanted crosstalk. The beam shape was measured via frequency scans for 10 ions and for 51 ions. Also, there was made a distinction between resonant and off-resonant excitation, since for

off-resonant excitation the aberrations are expected to be less distinct, since the beam profile is compressed in comparison to the resonant beam profile by a factor of $\sqrt{2}$. In fig. 4.3 one can see the spatial excitation profile for the ions 1 and 25 of a 51 ion string when being addressed resonantly.

For short enough pulses, the excitation does not saturate (i.e. it stays well below

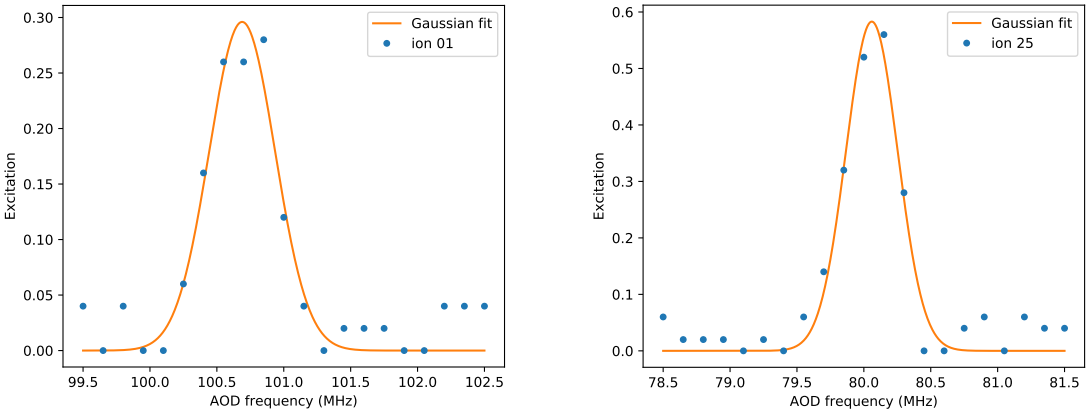

(a) **(b)**

Figure 4.3.: Transversal beam profiles for ions 1 (a) and ion 25 (b) when addressed resonantly. The excitation is plotted as a function of the AOD scanning frequency.

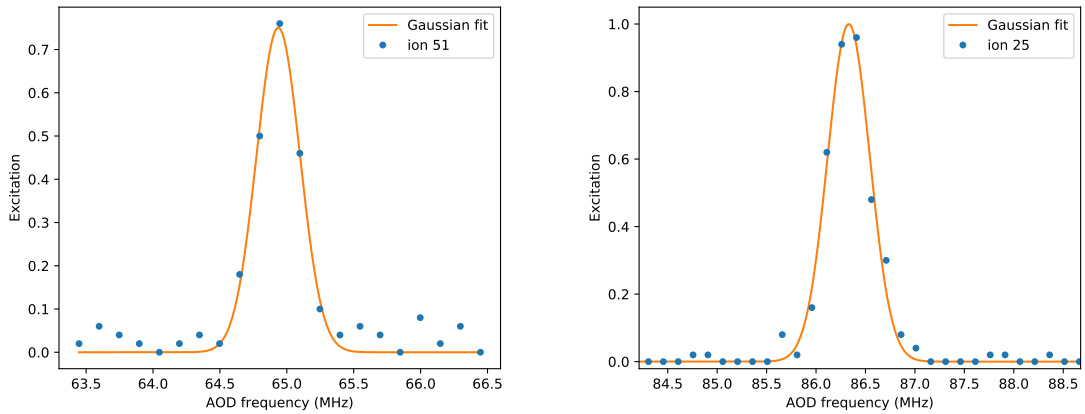

(a) **(b)**

Figure 4.4.: Transversal beam profiles for ions 51 (a) and ion 25 (b) when addressed off-resonantly. The excitation is plotted as a function of the AOD scanning frequency.

1) and in this case, the excitation probability $\sin(\frac{\Omega t}{2})^2$ can be approximated by $\frac{\Omega^2 t^2}{4}$, which is proportional to the intensity of the beam. Therefore, since the excitation does not show an exactly Gaussian shape in this regime, the same is true for the intensity

profile.
In the shown case, the profile has some features at the sides. Nevertheless, in the off-resonant case, they are less significant than in the resonant one. The off-resonant spatial excitation profile of ion 25 and ion 51 is shown in fig. 4.4. Ion 51 was chosen instead of ion 1 in order to make the excitation profile visible on both sides on the addressing range. Also, ion 1 and ion 51 are expected to behave similarly.
The difference in the behaviour on the wings of the excitation profile between resonant and off-resonant excitation can be seen quite clearly for the centre ions, whereas the ions at the edge seem to suffer from more aberrations. The reason for the stronger aberrations are thought to be the different focal lengths for the beams in the centre and at the edges of the addressing range. For beam spots not too far away from the focus, the beam profile was observed to be slightly aberrated. Most of these aberrations disappeared when going to the focus.
Also, for the outer ions, the excitation on the wings is suppressed not exactly as much as one would expect. The reason for this is that different ions were chosen in order to show the behaviour on both edges of the addressing range, whereby the behaviour seems to be slightly different.

4.3.2. Spot size

The most important parameter besides the addressing range is the spot size. The spot size was measured by analyzing the frequency scans made for 10 and 50 ions obtained with a resonant and off-resonant laser beam. The results for both resonant and off-resonant addressing can be seen in fig. 4.5 for 10 ions and fig. 4.6 for 50 ions. Hereby, in fig. 4.6 there was a 51 ion scan used for the resonant addressing. One may notice the different frequency axes for the scans. This is due to the fact, that the setup was slightly changed between the measurements. Amongst other things, the addressing range of the AOD was changed from $60 - 100\,\mathrm{MHz}$ to $70 - 110\,\mathrm{MHz}$, since there was a better performance observed there.
As one can see, the spot size is more or less the same over an addressing range of $234\,\mu\mathrm{m}$ for 51 ions.
In the centre of fig. 4.6a and fig. 4.6c, the spot size seems to be bigger than on the edges. This has on the one hand to do with the optimization of the focus. Due to different lengths of the beam path of the beams at the edges of the addressing range and the ones in the centre, the focal length is slightly different for them. If the focus is optimized for ion 51 or ion 1, the focus slightly changes (i.e., the spot size becomes bigger) for the centre ions. Another reason for this effect is, that the excitation on the sides doesn't go all the way up to 1, resulting in Gaussian fits with smaller amplitude and thus smaller width.
The main results of these plots are summed up in table 4.1. As one can see, the goal of a spot size of $2\,\mu\mathrm{m}$ was reached. The spot size was gained out of the FWHM by dividing it by $\sqrt{-2 \cdot \log \frac{1}{2}}$. This factor can be calculated quite easily by solving $e^{-\frac{x_{FWHM}^2}{2\omega^2}} = \frac{1}{2}$, where x_{FWHM} describes the x-value, which yields half of the maximum

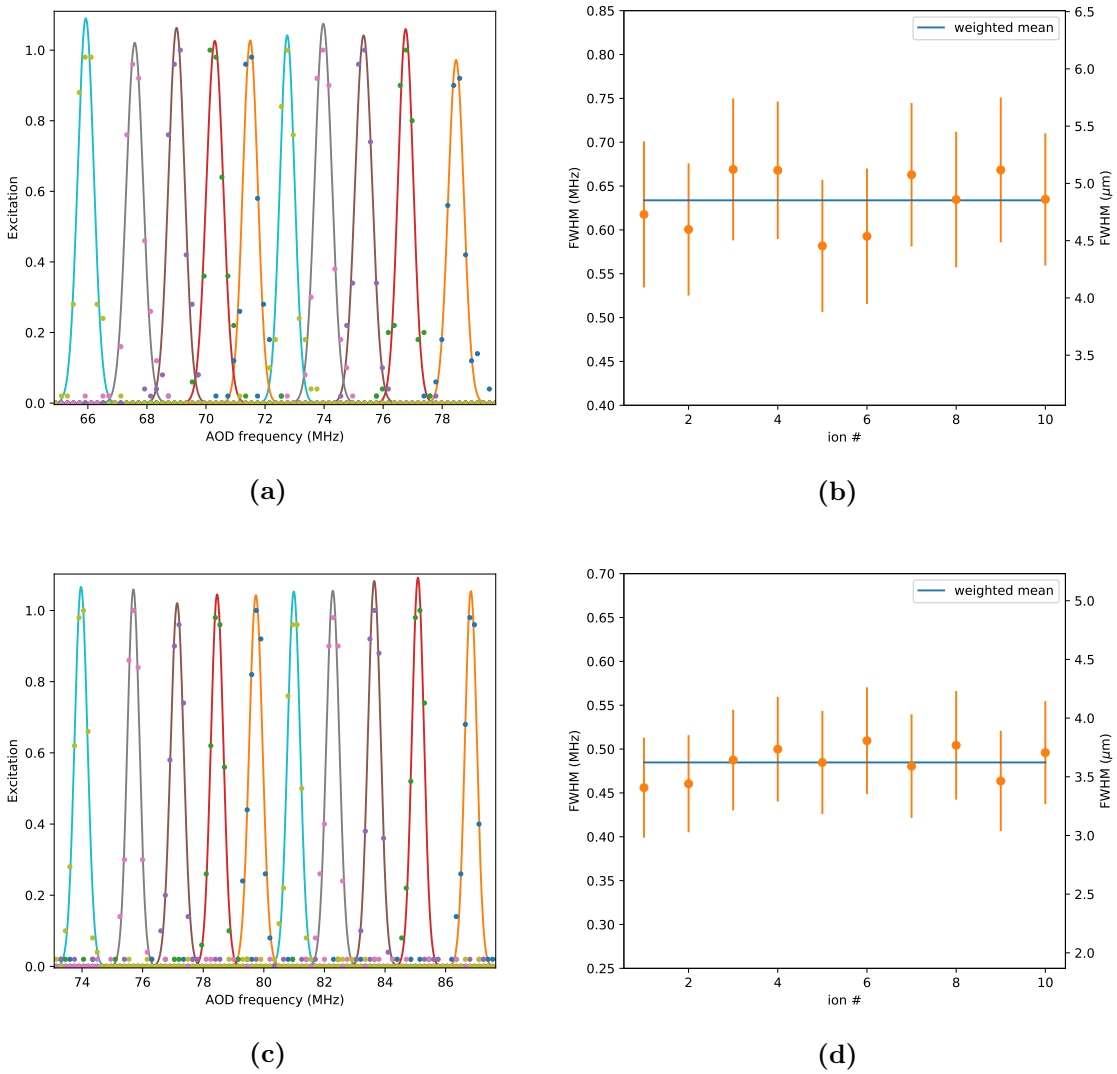

Figure 4.5.: Addressed frequency scans over a 10 ion string used for extracting the spot size of the addressing laser. A resonant addressing laser scan (a) yields the full-width half maxima shown in (b). Subpanels (c, d) show a similar experiment performed with an off-resonant addressing laser. The scans were made using π times of 2 µs for the resonant and 15 µs for the off-resonant excitation. The dots are the measured excitations, which were fitted using Gaussians. There were no error bars displayed in (a, c) for better visibility, but the errors were taken into account when fitting. Every point has an error of $\frac{1}{\sqrt{50}}$ due to quantum projection noise. The error bars in (b, d) are due to the fitting errors in (a, c). A weighted mean was made to extract the mean FWHM, which turned out to be 0.634 MHz, corresponding to 4.85 µm for (b) and 0.485 MHz, corresponding to 3.66 µm for (d). A trap frequency of 217 kHz was applied for the measurements.

y-value of a general Gaussian given by $y(x) = e^{-\frac{x^2}{2\omega^2}}$.
The FWHM resp. the spot sizes of a resonant and off-resonant excitation profile are

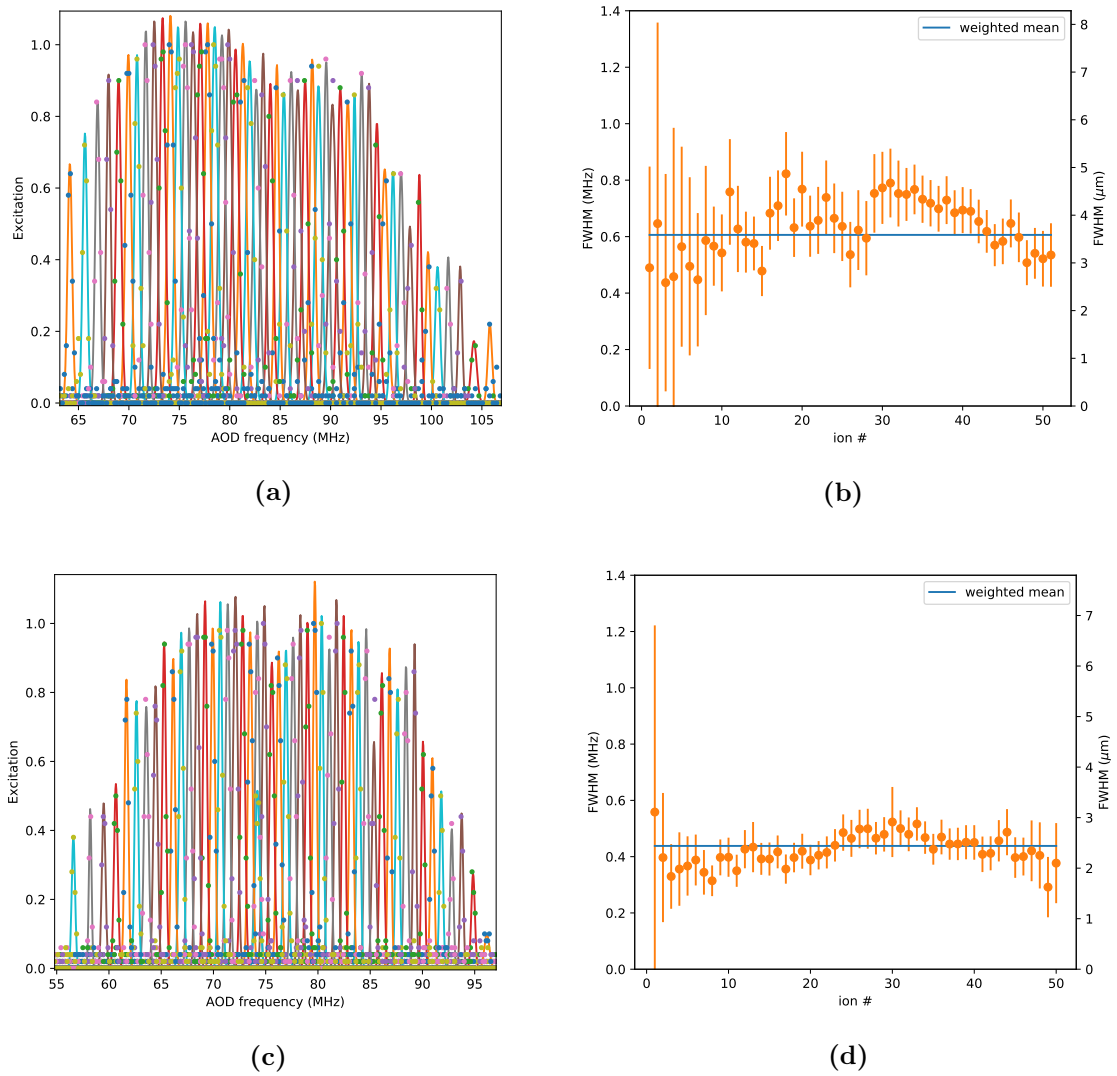

Figure 4.6.: Addressed frequency scans over a long ion string used for extracting the spot size of the addressing laser. A resonant addressing laser scan (a) yields the full-width half maxima shown in (b). Subpanels (c, d) show a similar experiment performed with an off-resonant addressing laser. The scans were made using π times of 15 µs for the resonant and 10 µs for the off-resonant excitation. The dots are the measured excitations, which were fitted using Gaussians. There were no error bars displayed in (a, c) for better visibility, but the errors were taken into account when fitting. Every point has an error of $\frac{1}{\sqrt{50}}$ due to quantum projection noise. The error bars in (b, d) are due to the fitting errors in (a, c). A weighted mean was made to extract the mean FWHM, which turned out to be 0.606 MHz, corresponding to 3.59 µm for (b) and 0.438 MHz corresponding to 2.44 µm for (d). A trap frequency of 137 kHz was applied.

expected to be connected by a factor of $\sqrt{2}$, since the width of a Gaussian (ideally corresponding to a resonant excitation profile) is broader by said factor with respect

to the same Gaussian squared (ideally corresponding to an off-resonant excitation profile). Looking at the corresponding values in table 4.1, one can see, that the relation differs from $\sqrt{2}$. The reason for this behaviour is that the measurements were taken on different days and with slightly shifted optics, since the setup was always optimized for requirements of the different measurements. Also, some effects appearing during taking measurements could only be solved by putting additional optics in the beam path, changing the effective focal length of the system, which then had to be compensated, mostly by moving the collimating lens.

Table 4.1.: Summary of the main results of fig. 4.5 and fig. 4.6. Hereby $\overline{\text{FWHM}}$ describes the mean FWHM and $2\bar{w}$ the mean spot size. The values in units of MHz have no error, since they arise from taking the mean value of the data shown in fig. 4.5b, fig. 4.5d, fig. 4.6b and fig. 4.6d, weighted with the according errors. The errors for the values in MHz result from fitting errors of the centres of the Gaussians in fig. 4.5a, fig. 4.5c, fig. 4.6a and fig. 4.6c when determining the frequency range the ions are spanned over, which is needed for converting the frequency into a length.

type of excitation	$\overline{\text{FWHM}}$ (MHz)	$\overline{\text{FWHM}}$ (µm)	$2\bar{w}$ (MHz)	$2\bar{w}$ (µm)
10 ions resonant	0.634	4.85(2)	0.542	4.15(2)
10 ions off-resonant	0.485	3.66(2)	0.415	3.13(2)
51 ions resonant	0.606	3.59(3)	0.518	3.07(2)
50 ions off-resonant	0.438	2,44(1)	0.374	2.09(1)

4.4. Crosstalk

When it comes to quantum simulation, the preparation of states is of major importance. The better the preparation, the better the result is. Therefore, one has to make sure, that when addressing one ion, the other ions are not affected by this. The main cause for such addressing errors is crosstalk with the nearest neighbour. This means, that by shooting a laser pulse at one ion, the ion(s) next to it are also addressed due to a too large beam profile or a broadened profile due to optical aberrations.

The method used in this thesis for quantifying crosstalk is the use of a resonant laser beam for the induction of Rabi oscillations on one ion and the observation the effect on the neighbouring ions. Since the laser intensity at the location of the other ions is much smaller, the Rabi frequency is smaller. The Rabi frequencies of the addressed ion and the neighbouring ions were fitted and the π time of the addressed ion was determined. The crosstalk of the neighbouring ions was defined to be the extent of excitation of the neighbouring ions at the π time of the addressed one, given in percent of the full excitation of 1. In fig. 4.8 the Rabi flops of ion 24, 25 and 26 are shown, when ion 25 is addressed in a 51 ion chain.

The Rabi oscillations were first made using a resonant addressing laser beam due to the high-frequency noise level of $2-4\,\%$ for the off-resonant addressing. In the case of the center ions, the crosstalk for the resonant beam is on the order of $2\,\%$ for ion

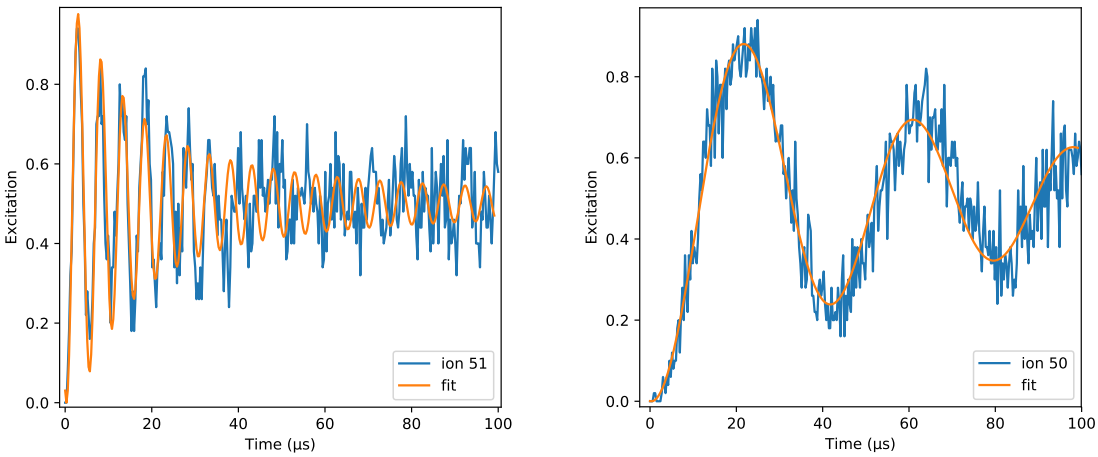

(a) **(b)**

Figure 4.7.: Rabi flops of ions 51 (a) and 50 (b) in a 51 ion chain, whereby ion 51 was addressed resonantly. The excitation curves were fitted using eq. 2.31, whereby for the fit of (a) only the first 100 data points were used. This was done due to the noise level of the rest of the data. All data points have an error due to quantum projection noise of $\frac{1}{\sqrt{50}}$, which was not displayed for better visibility.

24 and of 6 % for ion 26. For ions 23 and 27, the crosstalk is negligible. The exact numbers of the neighbouring ions can be found in table 4.2.
Of course, the crosstalk is bigger for a resonant beam in comparison to an off-resonant beam. The calculated values for the off-resonant beam are on the order of 0.37 % for ion 26 and 0.06 % for ion 24. Once the high-frequency noise was fixed, there was also actual data taken for off-resonant addressing, showing the crosstalk to be on the order of 0.45 % resp. 0.41 % for the corresponding ions. The corresponding data is displayed in fig. 4.10. Also here, all the exact calculated and measured numbers are given in table 4.2.
The same measurements were done addressing ion 1 resp. ion 51 and measuring Rabi flops for ion 2, 3, etc. resp. 50, 49, etc., whereby here, hardly any crosstalk was observed already in the case of resonant addressing. Rabi flops for ions 50 and 51, while ion 51 was addressed, are shown in fig. 4.7, Rabi flops for ion 1, 2, 3 and 4 in fig. 4.9. Off-resonant Rabi flops for ion 1, 2, 3 and 4 in a 54 ion chain are displayed in fig. 4.11.

The calculated values for the off-resonant crosstalk for the next neighbours are in the region of the calculated ones. The reason for not being the same is, that the position of the collimating lens was changed between the resonant and the off-resonant measurements, resulting in a different behaviour of the focal spot. The reason for the bigger crosstalk of the ions 49 and 48 with respect to ion 50 in the case of ion 51 being addressed should not be due to the laser beam having features in the focal plane at the position of these ions, since they are located quite far away (20 µm or more), but

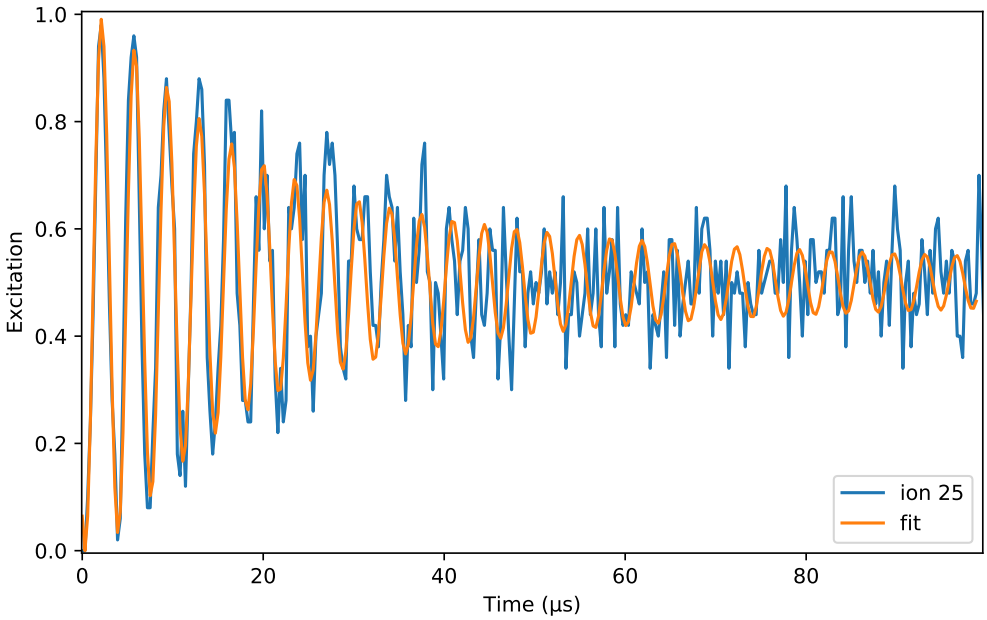

(a)

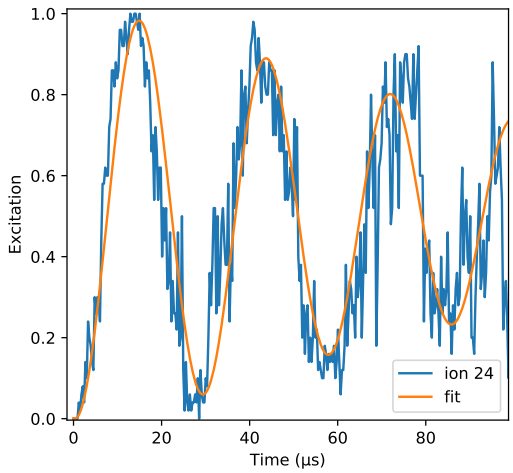

(b)

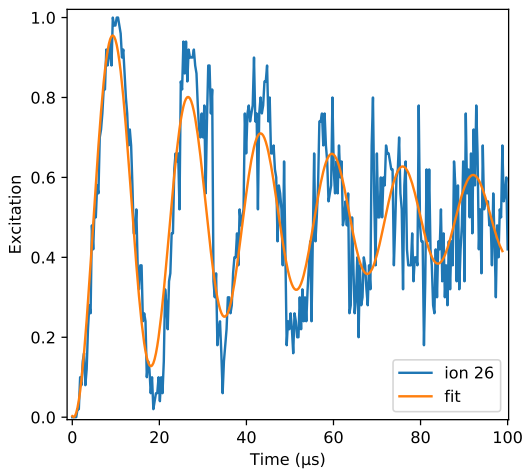

(c)

Figure 4.8.: Rabi flops of ions 24, 25 and 26 of a 51 ion chain when ion 25 is addressed. The Rabi flops of ion 25 are shown in (a), the ones of ion 24 resp. 26 in (b) resp. (c). Fits were made using eq. 2.31 in order to determine the nearest-neighbour crosstalk. All data points have an error due to quantum projection noise of $\frac{1}{\sqrt{50}}$, which was not displayed for better visibility.

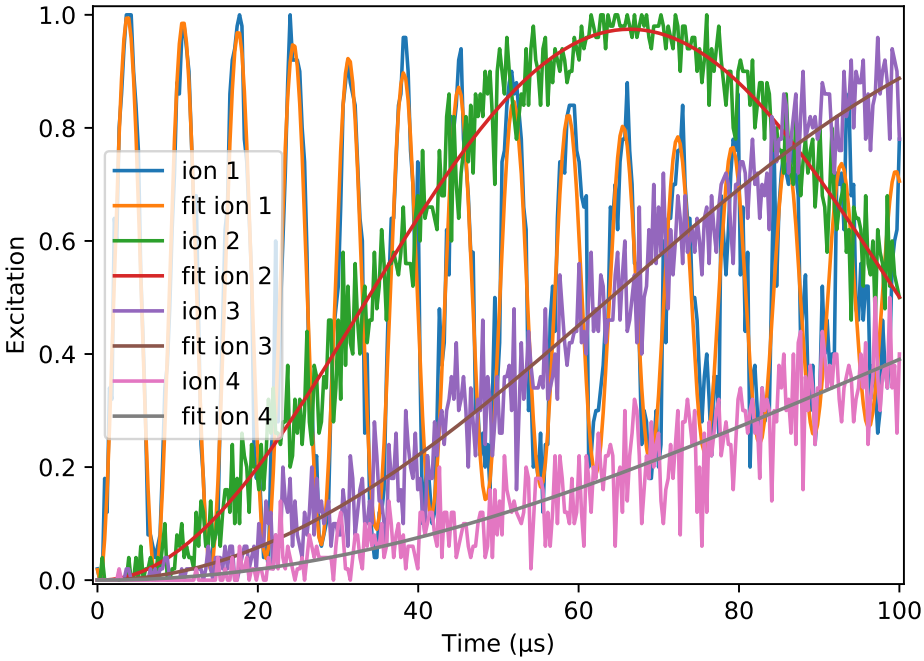

Figure 4.9.: Rabi flops of ion 1, 2, 3 and 4 of a 51 ion chain while ion 1 is addressed resonantly. The data was fitted using eq. 2.31, the π times and results for the crosstalk can be found in table 4.2. All the data points have an error due to quantum projection noise of $\frac{1}{\sqrt{50}}$, which was omitted in the plot for better visibility, but taken into consideration for the fits.

more likely due to detection errors.
As one can see, the Rabi oscillations are decaying with rising addressing pulse length. This is due to the fact, that the ions weren't cooled to their ground state of motion. Out of the fits using eq. 2.31, a Lamb-Dicke factor η on the order of $\eta \approx 0.05$ and a mean phonon number $\bar{n}$ of a few hundred phonons were extracted. The exact numbers can't be given, since the fitting error was too big, but since the most likely values were always in the same region for all the nearest-neighbour fits of the Rabi flops, the meaningfulness of these values can be stated at least to some extent.
The reason for the ions not being cooled to the ground state is, that the corresponding laser system wasn't adjusted for a 50 ion chain at the time the measurements were taken. Also, for the determination of nearest-neighbour crosstalk, the mean phonon number is not that important, as long as the number is low enough to allow for fitting of the Rabi oscillation curves.
Again, the same measurements were done for a 10 ion chain, the results can be found in table 4.3, some exemplary data sets are shown in the appendix A. As one can see, for a 10 ion chain the nearest-neighbour crosstalk is almost not existent. The reason for the crosstalk for 10 ions being much smaller with respect to 50 ions is, that the

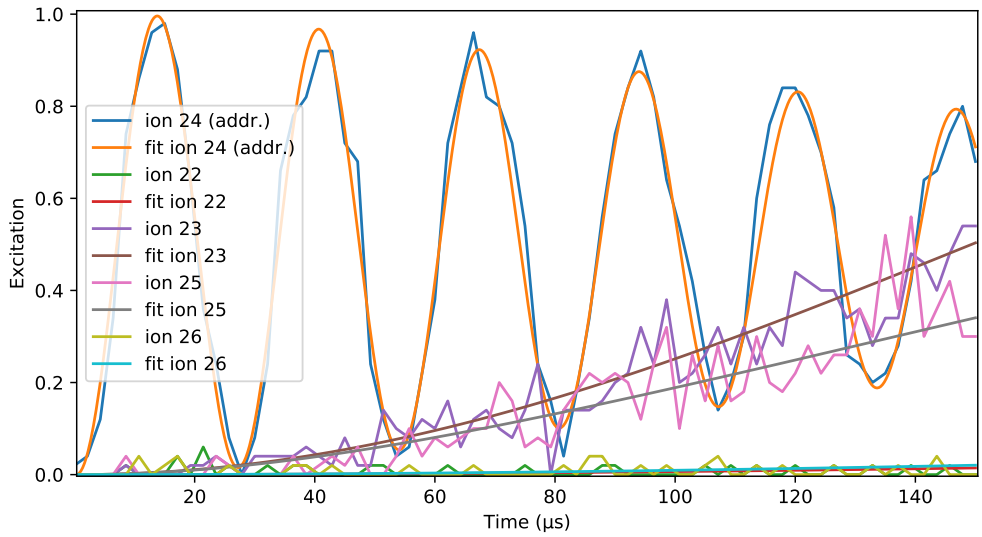

Figure 4.10.: Rabi flops of ions 22, 23, 24, 25 and 26 in a 51 ion chain, whereby ion 24 was addressed off-resonantly. The excitation curves were fitted using eq. 2.31. All data points have an error due to quantum projection noise of $\frac{1}{\sqrt{50}}$, which was not displayed for better visibility.

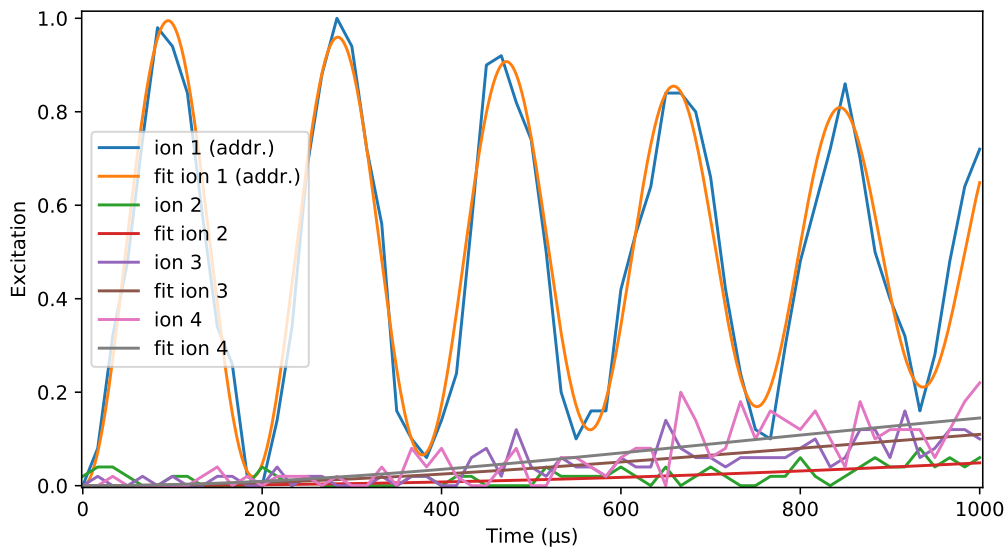

Figure 4.11.: Rabi flops of ions 1, 2, 3 and 4 in a 54 ion chain, whereby ion 1 was addressed off-resonantly. The excitation curves were fitted using eq. 2.31. All data points have an error due to quantum projection noise of $\frac{1}{\sqrt{50}}$, which was not displayed for better visibility.

distance between the ions is much bigger, namely 6.9 µm for 10 ions (and 217 kHz trap

Table 4.2.: Nearest neighbour crosstalk (CT) of the edge and centre ions in a 51 ion chain. The errors are due to fitting errors, if there are no errors specified, they are negligible (at least 1 order of magnitude smaller than the last digit of the value). The measured off-resonant data for ion 1 was taken for a 54 ion chain, the one for ion 25 was taken with ion 24 actually being the addressed one, meaning the ion number was shifted by 1.

ion #	CT resp. (%)	CT off-res. (%, calc.)	CT off-res. (%, meas.)	π time res. (µs)
ion 1				3.38(1)
ion 2	0.527	$2.78(2) \times 10^{-3}$	4.08×10^{-2}	60.5(2)
ion 3	0.144	$2.08(2) \times 10^{-4}$	0.138	127(1)
ion 4	4.70×10^{-2}	$2.21(2) \times 10^{-5}$	0.198	162(1)
ion 25				1.74(1)
ion 22	4.37×10^{-2}	$1.91(2) \times 10^{-5}$	2.7×10^{-5}	99(1)
ion 23	0.106	$1.23(1) \times 10^{-4}$	1.09×10^{-2}	62(1)
ion 24	2.36	$5.59(5) \times 10^{-2}$	0.445	13.5(1)
ion 26	6.04	0.365(3)	0.417	8.03(3)
ion 27	3.90×10^{-2}	$1.51(1) \times 10^{-5}$	1.57×10^{-2}	109(1)
ion 28	5.96×10^{-2}	$3.55(3) \times 10^{-5}$	3.56×10^{-5}	84.4(1)
ion 51				2.46(1)
ion 48	5.46×10^{-2}	$3.0(1) \times 10^{-5}$	1.04×10^{-2}	107(2)
ion 49	8.85×10^{-2}	$7.8(3) \times 10^{-5}$	1.51×10^{-2}	84(1)
ion 50	1.23	$1.51(1) \times 10^{-2}$	7.20×10^{-3}	18.3(2)

Table 4.3.: Nearest neighbour crosstalk of the edge and center ions in a 10 ion chain

ion #	crosstalk resonant (%)	crosstalk off-res. (%, calc.)	π time resonant (µs)
ion 1			1.86(1)
ion 2	0.127	$1.62(2) \times 10^{-4}$	69.1(6)
ion 3	1.17×10^{-2}	$1.38(1) \times 10^{-6}$	163(4)
ion 4	7.05×10^{-3}	$4.98(5) \times 10^{-7}$	293(9)
ion 5			1.65(1)
ion 2	2.03×10^{-2}	$4.11(4) \times 10^{-6}$	149(2)
ion 3	7.06×10^{-3}	$4.98(5) \times 10^{-7}$	252(7)
ion 4	5.64×10^{-2}	$3.19(3) \times 10^{-5}$	71.0(9)
ion 6	0.282	$7.92(8) \times 10^{-4}$	38.1(3)
ion 7	1.57×10^{-2}	$2.45(2) \times 10^{-6}$	120(3)
ion 8	3.98×10^{-3}	$1.58(2) \times 10^{-7}$	294(22)
ion 10			1.52(1)
ion 7	7.22×10^{-4}	$5.21(5) \times 10^{-9}$	714(133)
ion 8	1.71×10^{-2}	$2.93(3) \times 10^{-6}$	147(2)
ion 9	0.185	$3.41(3) \times 10^{-4}$	41.4(3)

frequency) compared to 3.7 µm for 51 ions (and 137 kHz trap frequency) for the center

ions. This means, that for this number of ions, one can program quantum gates of quite high fidelity, given that the state preparation etc. are also working on a low noise level.

4.5. Observation of beat signal

In this section, an effect, which was observed while taking measurements, is described. While resonantly exciting Rabi flops on the center ions of a 51 ion chain, the Rabi flops appeared to decay, which is not unusual, given that the ions didn't have 0 temperature. The decay of the Rabi flops corresponds to a decay of coherence. But after a certain time, the Rabi flops reappeared, meaning a revival of coherence, which should not be the case. An exemplary data set of the effect for the central ions of a 51 ion chain is displayed in fig. 4.12.

By putting a polariser into the setup before the AOD, the beat signal was slightly

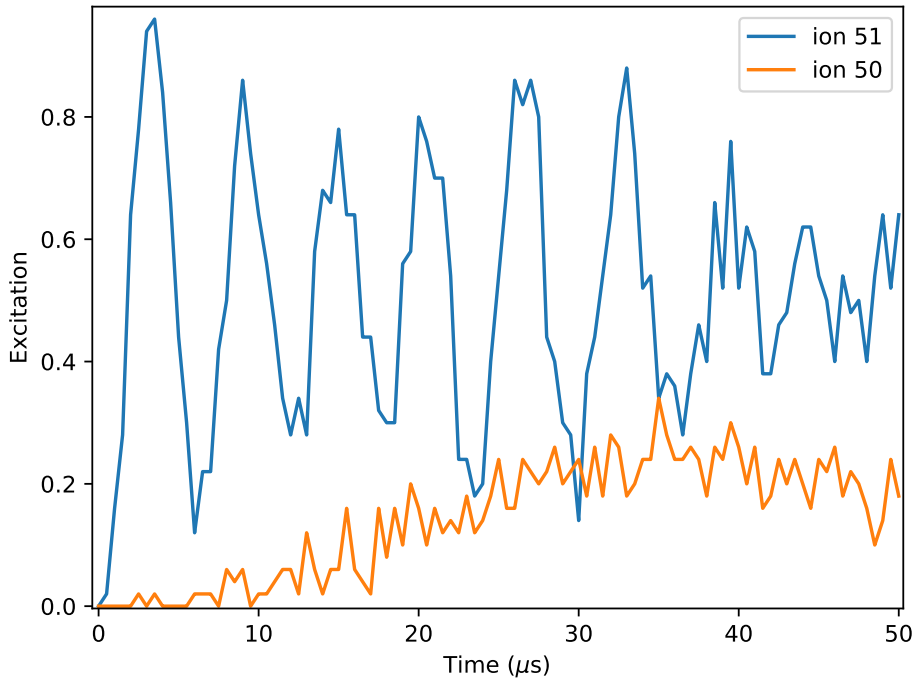

Figure 4.12.: Resonant excitation of ion 50 and 51 in a 51 ion chain as function of the addressing pulse length, driving the $m_j = 1/2 \rightarrow m_j = 5/2$ transition.

improved, but the problem could only be solved, when changing from the $m_j = 1/2 \rightarrow m_j = 5/2$ transition to the $m_j = 1/2 \rightarrow m_j = 3/2$ transition with m_j the quantum number of the magnetic Zeeman sublevel (see fig. 2.5). Up to the point of finishing this thesis, no satisfactory explanation of this effect can be given.

5. Conclusion and outlook

The goal of the thesis was setting up an optical system which allows for the addressing of a 50-ion chain with a spotsize on the order of 2 µm.
The first step towards this goal was the simulation of the optical system, which was done using the ZEMAX optics design software. By lining up 5 stock lenses before a custom-made objective, the simulations showed, that the goal stated above should be within reach.
At the same time, the AOD, which was already chosen and delivered before this project was started, was characterized, to be able to detect possible issues, which luckily didn't show up. The diffraction efficiency turned out to be as good as specified on the data sheet. The response time was in the region of a few microseconds and therefore good enough for the purpose of performing quantum simulation and the dependence on the RF power put into the AOD didn't show any irregularities.
Knowing this and the simulation results, the next step was the construction of a test of a test setup. At this stage, quite a bit of time was spent by efforts to measure the laser spot size by razor blade scans, which in the end didn't lead to the desired results, probably due to trembling of the razor blade, which can have quite an effect when it comes to the measuring of structures on a micrometer scale or even below. The problem was solved using a CCD camera with a pixel size of $1.67\,\mu\text{m} \times 1.67\,\mu\text{m}$. With the help of this camera and the knowledge of how the waist of a Gaussian beam evolves around the focus, the focal spot of the laser after running through the test setup was determined to be as small as 2 µm and therefore as small as it was in the setup used in the addressing setup previously used in the trapped-ion experiment. Also, by measuring the separation in pixels of two laser beams deflected, applying the border frequencies of the specified $60 - 100\,\text{MHz}$ range, an addressing range of 200 µm could be proofed.
For possible use in future experiments, the behaviour of the AOD output for multiple input frequencies, mostly the optical mixing effects, was investigated. For the purpose of quantum simulation, these effects might be too large, but at the same time they were visible only at high RF-powers. So by going to lower RF-powers and compensating the lower diffraction efficiency by a higher laser power, this effect might be reduced.
After mounting the new system in the experiment for the first time, the desired result of a 200 µm addressing range (as it was achieved in the test setup) was missed by several tens of microns. Also, discussions revealed, that for a suitable tip voltage of the trap, the chain length had to be on the order of 230 µm for 50 ions. Solving both problems at the same time, simulations for an addressing range of 280 µm were done, leading to the required movability of the laser focal spot on the ion chain. The reasons for this problem are thought to be on the one hand a difference between the objective

used in the simulations and the actual objective built into the experiment and on the other hand differences in the distances between collimating lens and objective resp. objective and ions with respect to the test setup.
In the experiment, the spot size could be determined again to be as small as 2 µm, with off-resonant crosstalk in the center of a 51 ion chain on the order of 0.4 %, which is a good basis for performing quantum simulations. On the edges of these long chains and for chains containing fewer ions, the crosstalk with the nearest neighbouring ions is vanishing. The measurements for the determination of the off-resonant crosstalk were first done using a resonant laser beam on the ions, since the obvious determination of the crosstalk using a off-resonant laser beam was only made possible 3 months later after fixing high-frequency noise of the laser of the laser on the order of a few percent, which would have made it impossible to distinguish this noise from the actual crosstalk.
Summarising, it can be stated, that the goal of being able to address a chain of 50 ions with a laser beam of 2 µm spot size was reached.
At the moment, soft- and hardware issues hinder the preparation of a sequence of pulses to be performed on the ions, in order to e.g. prepare a Néel state (a sequence of ions being alternately in the ground and excited state) or, which is the actual purpose of the experiment, doing quantum simulation.
Nevertheless, this thesis shows, that in principle quantum simulation with single-ion control is possible on a string of 50 (or even more) ions, which is important for the scalability not only of quantum simulators, but also for quantum computers based on cold trapped ions. The research towards a commercially available quantum computer is, at least in my opinion, as active as never before, since not only the big players invest in quantum science, but also more and more small startups are dedicating their work to quantum technology.

Bibliography

[1] Alan Mathison Turing. On Computable Numbers, with an Application to the Entscheidungsproblem. *Proceedings of the London Mathematical Society*, 42:230–265.

[2] Werner Heisenberg. Über quantentheoretische Umdeutung kinematischer und mechanischer Beziehungen. *Z. Physik*, 33:879–893, 1925.

[3] Erwin Schrödinger. Quantisierung als Eigenwertproblem I. *Annalen der Physik*, 79:361–376, 1926.

[4] Richard Phillips Feynman. Simulating Physics with Computers. *International Journal of Theoretical Physics*, 21:467–488, 1982.

[5] Lov Groover. A fast quantum mechanical algorithm for database search. In *28th Annual ACM Symposium on the Theory of Computing*, 1996.

[6] Peter W Shor. Polynomial-Time Algorithms for Prime Factorization and Discrete Logarithms on a Quantum Computer. *SIAM Journal on Computing*, 26:1484–1509, 1997.

[7] Juan Ignacio Cirac and Peter Zoller. Quantum Computations with Cold Trapped Ions. *Phys. Rev. Lett.*, 74:4091, 1995.

[8] Ferdinand Schmidt-Kaler, Hartmut Häffner, Mark Riebe, Stephan Gulde, Gavin P. T. Lancaster, Thomas Deuschle, Christoph Becher, Christian F. Roos, Jürgen Eschner, and Rainer Blatt. Realization of the Cirac–Zoller controlled-NOT quantum gate. *Nature*, 422:408–411, 2003.

[9] Lieven M. K. Vandersypen, Matthias Steffen, Gregory Breyta, Costantino S. Yannoni, Mark H. Sherwood, and Isaac L. Chuang. Experimental realization of Shor's factorizing algorithm using nuclear magnetic resonance. *Nature*, 414:883–887, 2001.

[10] H. Häffner, W. Hänsel, C. F. Roos, J. Benhelm, D. Chek-al kar, M. Chwalla, T. Körber, U. D. Rapol, M. Riebe, P. O. Schmidt, C. Becher, O. Gühne, W. Dür, and R. Blatt. Scalable multiparticle entanglement of trapped ions. *Nature*, 438:643–646, 2005.

[11] Thomas Monz, Philipp Schindler, Julio T. Barreiro, Michael Chwalla, Daniel Nigg, William A. Coish, Maximilian Harlander, Wolfgang Hänsel, Markus

Hennrich, and Rainer Blatt. 14-Qubit Entanglement: Creation and Coherence. *Phys. Rev. Lett.*, 106:130506, 2011.

[12] Davide Castelvecchi. Quantum computers ready to leap out of the lab. *Nature*, 541:9–10, 2017.

[13] Immanuel Bloch, Jean Dalibard, and Sylvain Nascimbène. Quantum simulations with ultracold quantum gases. *Nat. Phys.*, 8:267–276, 2012.

[14] Christian Gross and Immanuel Bloch. Quantum simulation with ultracold atoms in optical lattices. *Science*, 357:995–1001, 2017.

[15] David P. DiVincenzo. The Physical Implementation of Quantum Computation. *Progress of Physics*, 48:771–783, 2000.

[16] Colin D. Bruzewicz, John Chiaverini, Robert McConnell, and Jeremy M. Saged. Trapped-ion quantum computing: Progress and challenges. *Applied Physics Reviews*, 6:021314, 2019.

[17] Anders Sørensen and Klaus Mølmer. Multi-particle entanglement of hot trapped ions. *Phys. Rev. Lett.*, 82:1835, 1999.

[18] Nicolai Friis, Oliver Marty, Christine Maier, Cornelius Hempel, Milan Holzäpfel, Petar Jurcevic, Martin B. Plenio, Marcus Huber, Christian Roos, Rainer Blatt, and Ben Lanyon. Observation of Entangled States of a Fully Controlled 20-Qubit System. *Phys. Rev. X*, 8:021012, 2018.

[19] Frans Michel Penning. Die Glimmentladung bei niedrigem Druck zwischen koaxialen Zylindern in einem axialen Magnetfeld. *Physica*, 3:873–894, 1936.

[20] Wolfgang Paul and Helmut Steinwedel. Ein neues Massenspektrometer ohne Magnetfeld. 8a:448–450, 1953.

[21] J.E. Campana. Elementary theory of the quadrupole mass filter. *International Journal of Mass Spectrometry and Ion Physics*, 33:101–117, 1980.

[22] Samuel Earnshaw. On the Nature of the Molecular Forces which Regulate the Constitution of the Luminiferous Ether. *Trans. Camb. Phil. Soc.*, 7:97–112, 1842.

[23] Wolfgang Paul. Electromagnetic traps for charged and neutral particles. *Rev. Mod. Phys.*, 62:531–540, 1990.

[24] Émile L. Mathieu. Memoire sur le Mouvement Vibratoire d'une Membrane de Forme Elliptique. *Journal de Mathématiques Pures et Appliquées*, 13:137–203, 1868.

[25] D.F.V. James. Quantum dynamics of cold trapped ions with application to quantum computation. *Applied Physics B*, 66:181–190, 1998.

[26] Cornelius Hempel. *Digital quantum simulation, Svhrödinger cat state spectroscopy and setting up a linear ion trap.* PhD thesis, University of Innsbruck/Institut für Quantenoptik und Quanteninformation, 2014.

[27] NIST Atomic Data for Calcium. `https://physics.nist.gov/PhysRefData/Handbook/Tables/calciumtable1.htm`. Accessed:05.07.2019.

[28] Gerhard Kirchmair. *Quantum non-demolition measurements and quantum simulation.* PhD thesis, University of Innsbruck, 2010.

[29] Christian Felix Roos. *Controlling the quantum state of trapped ions.* PhD thesis, University of Innsbruck, 2000.

[30] Paul Adrien Maurice Dirac. *The Principles Of Quantum Mechanics.* Oxford Science Publications, 1939.

[31] Tito Arecchi and Rodolfo Bonifacio. Theory of optical maser amplifiers. *IEEE Journal of Quantum Electronics*, 1:169–178, 1965.

[32] Stanley Howard Autler and Charles Hard Townes. Stark Effect in Rapidly Varying Fields. *Physical Review*, 100:703–722, 1955.

[33] Manoj Kumar Joshi. *Coherent Dynamiccs of Trapped Ions Within and Outside the Labm-Dickie Regime.* PhD thesis, Imperial College London, 2018.

[34] Bahaa E. A. Saleh and Malvin C. Teich. *Fundamentals of Photonics.* John Wiley & Sons Inc, Hoboken, New Jersey, second edition, 2007.

[35] David Hilbert, John von Neumann, and Lothar Nordheim. Über die Grundlagen der Quantenmechanik. *Mathematische Annalen*, 98:1–30, 1928.

[36] S. Lloyd. Universal Quantum sImulators. *Science*, 273:1073–1078, 1996.

[37] Rainer Blatt and Christian Felix Roos. Quantum simulations with trapped ions. *Nat. Phys.*, 8:277–284, 2012.

[38] Benjamin Peter Lanyon et al. Universal Digital Quantum Simulation with Trapped Ions. *Science*, 334:57–61, 2011.

[39] C. Kokail, C. Maier, R. van Bijnen, T. Brydges, M. K. Joshi, P. Jurcevic, C. A. Muschik, P. Silvi, R. Blatt, C. F. Roos, and P. Zoller. Self-verifying variational quantum simulation of lattice models. *Nature*, 569:355–360, 2019.

[40] W. M. Itano, J. C. Bergquist, J. J. Bollinger, J. M. Gilligan, D. J. Heinzen, F. L. Moore, M. G. Raizen, and D. J. Wineland. Quantum projection noise: Population fluctuations in two-level systems. *Phys. Rev. A*, 47:3554, 1995.

[41] M. H. Quenouille. Notes on bias in estimation. *Biometrika*, 43:353–360, 1956.

[42] Philipp Schindler et al. A quantum information processor with trapped ions. *New J. Phys.*, 15:123012, 2013.

[43] Radiant ZEMAX LLC. *ZEMAX Optical Design Program User's Manual*, 2011.

[44] Jan Benhelm. *Precision Spectroscopy and Quantum Information Processing with Trapped Calcium Ions*. PhD thesis, University of Innsbruck, 2008.

[45] Fiber Collimators 60FC. `https://www.sukhamburg.com/download/FiberCollimators60FC.pdf`. Accessed: 30.07.2019.

[46] CONEX-NSA12 Actuator User's Manual. `https://www.newport.com/medias/sys_master/images/images/h71/h05/9134493892638/CONEX-NSA12-User-s-Manual.pdf`. Accessed:30.07.2019.

[47] N-BK7 Plano-Convex Lenses (AR Coating: 650-1050 nm). `https://www.thorlabs.com/NewGroupPage9.cfm?ObjectGroup_ID=3280`. Accessed:30.07.2019.

[48] KPC043AR.16 Technical Specs. `https://www.newport.com/p/KPC043AR.16`. Accessed:30.07.2019.

[49] ZHL-1-2-W Coaxial Amplifier. https://ww2.minicircuits.com/pdfs/ZHL-1-2W.pdf. Accessed:30.07.2019.

Appendices

A. Rabi flops in a 10 ion chain

Below, addressed Rabi flops on ions 1, 5 and 10 of a 10 ion chain are shown. Hereby, also the Rabi flops of the neighbouring ions are displayed. The π times, resonant and off-resonant crosstalks are listed in table 4.3. The fits were made using eq. 2.31, whereby for all data points an error of $\frac{1}{\sqrt{50}}$ due to quantum projection noise was taken into account. The Lamb-Dicke factor η is on the order of $\eta \approx 0.1$ for the ions shown, the mean phonon number $\bar{n}$ is on the order of $\bar{n} \approx 100$.

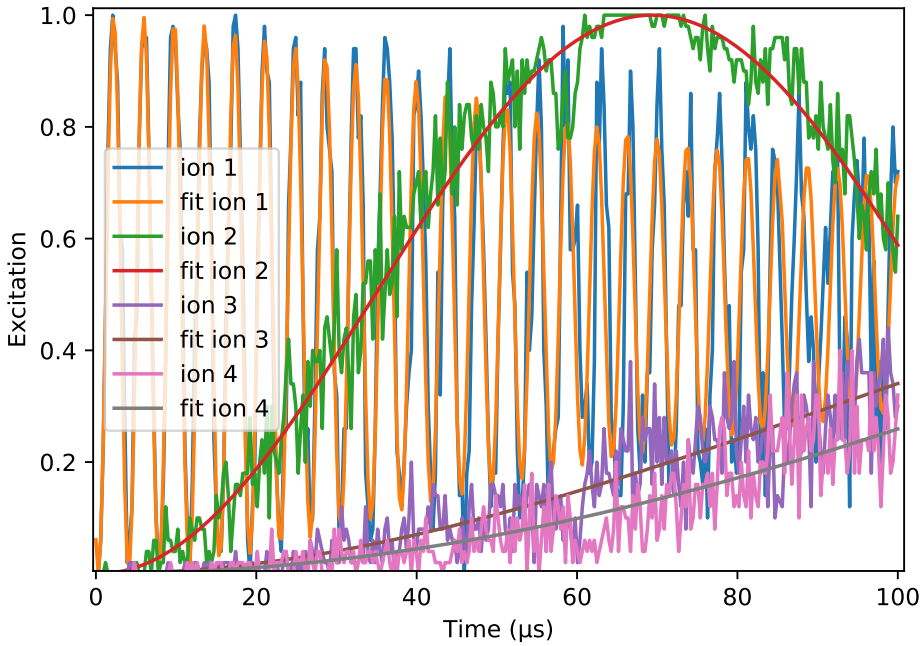

Figure A.1.: Rabi flops on ions 1, 2, 3, and 4 of a 10 ion chain while ion 1 was addressed resonantly. Errors of the data points of $\frac{1}{\sqrt{50}}$ due to quantum projection noise were omitted for better visibility.

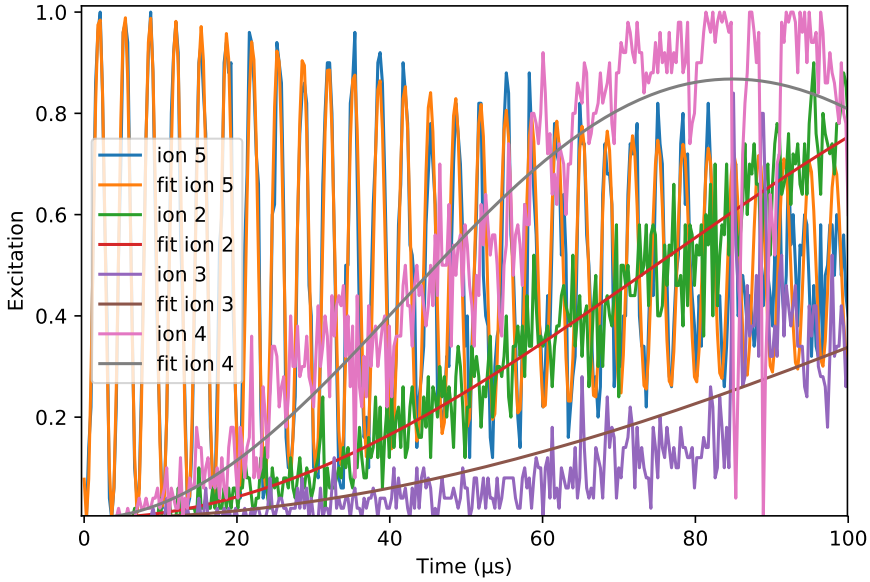

Figure A.2.: Rabi flops on ions 2, 3, 4 and 5 of a 10 ion chain while ion 5 was addressed resonantly. Errors of the data points of $\frac{1}{\sqrt{50}}$ due to quantum projection noise were omitted for better visibility.

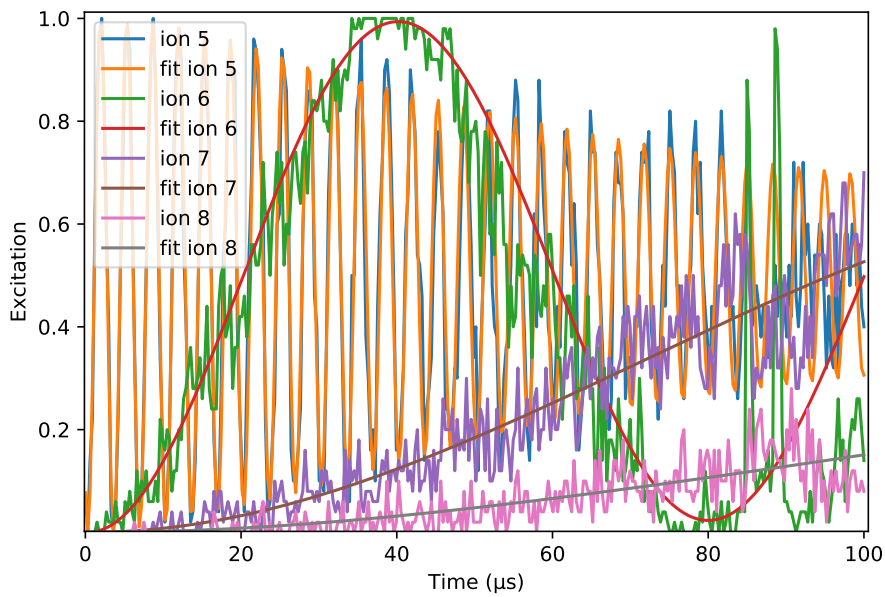

Figure A.3.: Rabi flops on ions 5, 6, 7 and 8 of a 10 ion chain while ion 5 was addressed resonantly. Errors of the data points of $\frac{1}{\sqrt{50}}$ due to quantum projection noise were omitted for better visibility.

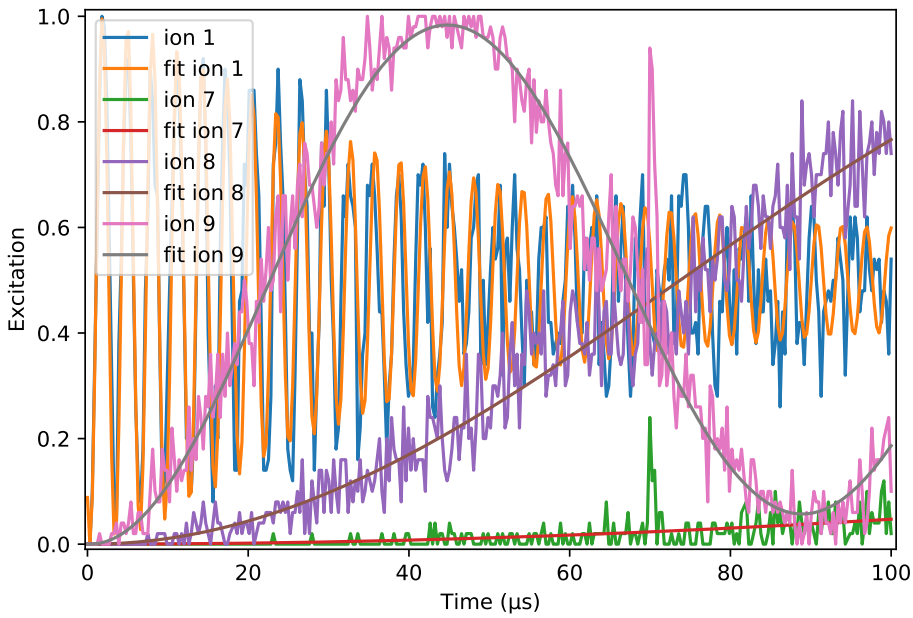

Figure A.4.: Rabi flops on ions 7, 8, 9, and 10 of a 10 ion chain while ion 10 was addressed resonantly. Errors of the data points of $\frac{1}{\sqrt{50}}$ due to quantum projection noise were omitted for better visibility.

B. Datasheet AOD

Below, the data sheet of the AOD used in this thesis is shown. As one may see, the AOD wasn't specifically made for the usage with 729 nm laser light, nevertheless the performance was satisfactory. This should also be the case, since the specified operating wavelength of $750 - 850$ nm doesn't lie far away from the laser wavelength put into the AOD.
Also, the RF bandwidth was seen to be usable in a broader range than specified on the datasheet, RF frequencies of 110 MHz and more delivered nice results as well as frequencies of 50 MHz

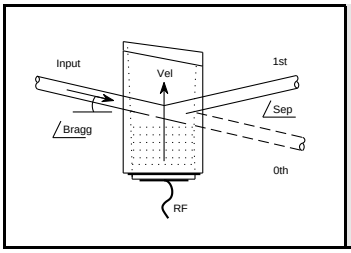

LS55-NIR

Acousto-Optic Deflector

1106

SPECIFICATIONS

Operating Wavelength:	750nm to 850nm
Interaction Material:	TeO_2 (Slow Shear Mode)
Active Aperture:	2mm H x 7mm L
Centre Frequency (f_c)	80MHz
RF Bandwidth (Δf)	40MHz
Input Impedance:	50Ω (Nominal)
VSWR:	< 1.5 : 1 @ 80 MHz
Access Time (τ):	11.3μs
$\tau\Delta f$ Resolution:	450 Spots
Laser Polarization:	RH Circular (Preferred) / Linear

PERFORMANCE vs. WAVELENGTH

Wavelength (nm):	750	850
RF Drive Power (Watts):	<1.0	<1.0
Bragg Angle (mrad @ 80MHz)	48.6	55.1
Beam Separation (mrad) @ 80 MHz:	97.2	110.0
Scan Angle (Degrees):	2.78º	3.15º
Diffraction Efficiency (% @ 80MHz):	≥80.0	≥80.0

OUTLINE DRAWING

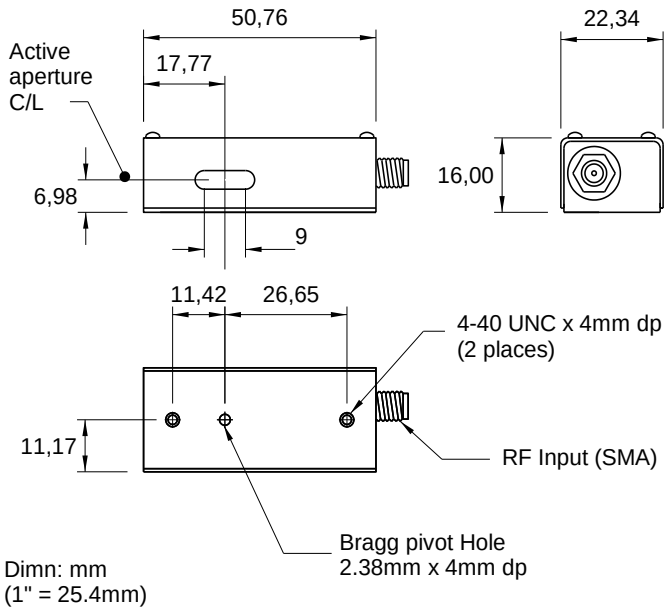

ALL SPECIFICATIONS SUBJECT TO CHANGE WITHOUT NOTICE
ISOMET CORP, 5263 Port Royal Rd, Springfield, VA 22151, USA.
Tel: (703) 321 8301 Fax: (703) 321 8546
E-mail: ISOMET@ ISOMET.COM ***Web Page: WWW.ISOMET.COM***

Quality Assured.
In-house: Crystal Growth,
Optical Polishing,
A/R coating, Vacuum Bonding

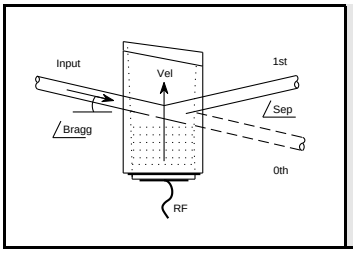

LS55-NIR

Acousto-Optic Deflector

1106

Recommended Driver

620C-80 (VARIABLE FREQUENCY & DIGITAL MOD'N)
630C-80 (VARIABLE FREQUENCY & ANALOG MOD'N))

Typical First Order Diffraction Efficiency vs. Frequency Response

R.H. Circular Polarization
(λ/4 waveplate not provided)

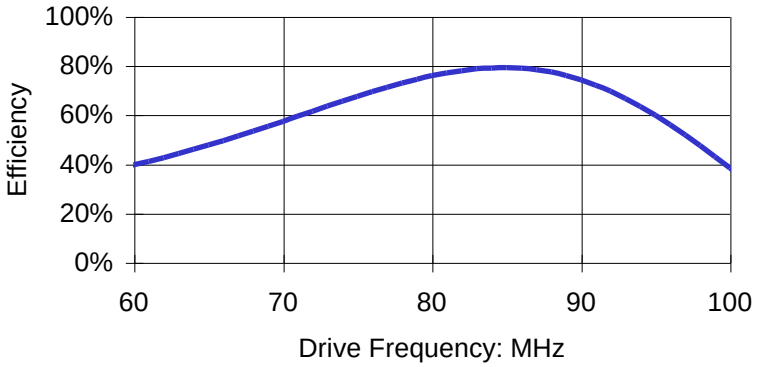

Linear Polarization

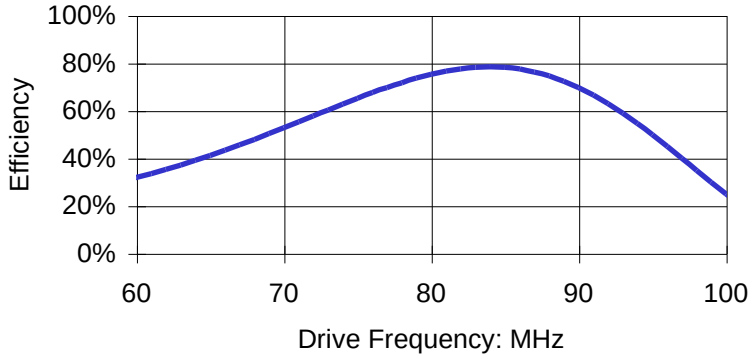

ALL SPECIFICATIONS SUBJECT TO CHANGE WITHOUT NOTICE
ISOMET CORP, 5263 Port Royal Rd, Springfield, VA 22151, USA.
Tel: (703) 321 8301 Fax: (703) 321 8546
E-mail: ISOMET@ ISOMET.COM ***Web Page: WWW.ISOMET.COM***

Quality Assured.
In-house: Crystal Growth,
Optical Polishing,
A/R coating, Vacuum Bonding

Acknowledgements

In the end of this thesis, I'd like to say thank you to a few people, without whom the making of this thesis wouldn't have been possible. First of all, I'd like to thank my parents and family, for the financial and whichever support, enabling me to stay focussed on physics during the semester. The second big thank you is owed to Prof. Rainer Blatt and Dr. Christian Roos, for the warm welcome in the big Blatt group and the possibility of carrying out my master thesis in an extraordinary research environment like the IQOQI. I also owe a big thank you to the Qsim team, Ben, Christine, Tiff and especially Manoj, who were always available and motivated to answer my tiring questions, may it be in the lab or the office. Talking of lab and office, it was Marco I spent the most time with, which was always much fun and made it at the same time possible to refresh and enlarge my Italian language skills.
Day by day, a great work is done behind the scenes by the administrative staff and the people in the mechanical workshop, who try to fulfil every wish even of a newly master student.
Last but not least, a big thank is owed to the 'Huppe', a bunch of people I've spent a large amount of my free time with during my studies, be it in Innsbruck or be it at home in South Tyrol. And, very last and even less least, to Mira, whom I've learned to know during my thesis and who nicely crowded my room in the last months :)

Eidesstattliche Erklärung

Ich erkläre hiermit an Eides statt durch meine eigenhändige Unterschrift, dass ich die vorliegende Arbeit selbständig verfasst und keine anderen als die angegebenen Quellen und Hilfsmittel verwendet habe. Alle Stellen, die wörtlich oder inhaltlich den angegebenen Quellen entnommen wurden, sind als solche kenntlich gemacht.

Die vorliegende Arbeit wurde bisher in gleicher oder ähnlicher Form noch nicht als Magister-/Master-/Diplomarbeit/Dissertation eingereicht.

Datum	Unterschrift